States of in-situ stress in the Duvernay East Shale Basin and Willesden Green of Alberta, Canada: variable in-situ stress states effect fault stability

Luyi W Shen[1,1], Douglas Ray Schmitt[2,2], Ruijia Wang[3,3], and Tyler E. Hauck[4,4]

[1]Department of Physics, University of Alberta
[2]Purdue University
[3]University of New Mexico
[4]Alberta Geological Survey

November 30, 2022

Abstract

Fault slip is controlled by the normal and shear tractions on a fault plane. A full understanding of the factors influencing induced seismicity requires quantitative knowledge of the in-situ stress tensor and fluid pressure. We analyze these variables for a 200 km $\times$ 200 km region with active hydraulic fracturing near the city of Red Deer, Canada. The levels of induced seismicity in the area were generally low before Mar 04, 2019, MW 3.8/ML 4.2 event that local residents felt. We use geophysical logs and pressure tests within the targeted Duvernay Formation to construct maps of ambient pore pressure, vertical and minimum horizontal stresses. Maximum horizontal stress is constrained from the focal mechanism inversion and borehole-based estimation method. We find a broad range of orientations are susceptible to slip and small perturbations of fluid pressure would promote displacement. This suggests that the differential variations in pore fluid pressure in the target formation may provide a metric of slip susceptibility; a map for the study area is developed. Areas of high susceptibility correlate with those experiencing higher levels of induced seismicity except for the Willesden Green oil field that has similarly elevated susceptibility and active hydraulic fracturing operations. The methods and results demonstrate how more quantitively constrained in-situ stresses developed from an ensemble of real field measurements can assist in assessing fault stability and in developing metrics for slip susceptibility.

States of in-situ stress in the Duvernay East Shale Basin and Willesden Green of Alberta, Canada: variable in-situ stress states effect fault stability

Luyi W. Shen[1,2*], Douglas R. Schmitt[1†], Ruijia Wang[4], Tyler E. Hauck[2]

[1]Institute of Geophysical Research, Department of Physics, University of Alberta, Edmonton, Canada

[2]Alberta Geological Survey, Alberta Energy Regulator, Edmonton, Alberta, Canada

[†]Now at Department of Earth, Atmospheric and Planetary Science, Purdue University, West Lafayette, Indiana, U.S.

[4]Department of Earth and Planetary Science, University of New Mexico, Albuquerque, U.S.

[*]Corresponding author: Luyi W. Shen (luyi@ualberta.ca)

Key Points:

- Quantitative measurements for the stress tensor and pore pressure in an area with active hydraulic fracturing and induced seismicity.
- Direct application of the stress tensor to understand factors controlling a recent earthquake linked to hydraulic fracturing.
- A stability map is built based on the difference between the formation pore pressure and critical fluid pressure that slips fault.

Abstract

Fault slip is controlled by the normal and shear tractions on a fault plane. A full understanding of the factors influencing induced seismicity requires quantitative knowledge of the in-situ stress tensor and fluid pressure. We analyze these variables for a 200 km × 200 km region with active hydraulic fracturing near the city of Red Deer, Canada. The levels of induced seismicity in the area were generally low before Mar 04, 2019, M_W 3.8/M_L 4.2 event that local residents felt. We use geophysical logs and pressure tests within the targeted Duvernay Formation to construct maps of ambient pore pressure, vertical and minimum horizontal stresses. Maximum horizontal stress is constrained from the focal mechanism inversion and borehole-based estimation method. We find a broad range of orientations are susceptible to slip and small perturbations of fluid pressure would promote displacement. This suggests that the differential variations in pore fluid pressure in the target formation may provide a metric of slip susceptibility; a map for the study area is developed. Areas of high susceptibility correlate with those experiencing higher levels of induced seismicity except for the Willesden Green oil field that has similarly elevated susceptibility and active hydraulic fracturing operations. The methods and results demonstrate how more quantitively constrained in-situ stresses developed from an ensemble of real field measurements can assist in assessing fault stability and in developing metrics for slip susceptibility.

1 Introduction

Globally, anthropogenically-induced earthquakes (up to M = 5 near some densely populated areas) in the past decade brought much attention to the risks and hazards associated with the injection [e.g., hydraulic fracturing, *Schultz et al.*, 2020 *Atkinson et al.,* 2020; waste disposal, *Hincks et al.*, 2018; geothermal, *Eberhart-Phillips and Oppenheimer*, 1984; *Ellsworth et al.,* 2019] and, to a lesser extent, extraction of masses [e.g., *Maury et al.*, 1992; *van Thienen-Visser and*

Breunese, 2015; *Wetmiller*, 1986] into/from the subsurface. Extensive efforts have been expended, mainly through the lenses of seismology, to better understand this phenomena with various triggering mechanisms proposed and investigated. Nevertheless, these reports, attempting to correlate earthquakes temporally and spatially with industrial activities, are primarily statistical in nature. There are very few exceptions based on the deterministic geomechanical observations [e.g., *Deng et al.*, 2016; *McClure and Horne*, 2011; *Shen et al.*, 2019b; *Stork et al.*, 2018; *Ameen* 2016].

Despite the elevated societal concerns, only a small fraction of the hydraulic fracturing (HF) operations results in moderate earthquakes (M > 2). Wells associated with induced earthquakes are classified as being 'seismogenic' [e.g., *Atkinson et al.*, 2016; *Schultz et al.*, 2018]; the absence of triggered earthquakes in most other HF wells is loosely attributed to 'varying geological conditions.' To date, the cause of such discrepancies is not well understood, but this is not surprising as statistical correlation requires the input of past earthquake records that would be absent for aseismic areas or areas not covered by seismometer networks. Techniques like Probabilistic Seismic Hazard Analysis rely on establishing statistical or empirical patterns of reported earthquake events [*Castaños and Lomnitz*, 2002] and show deficiencies in areas that were mapped with low risk but later experienced major, devastating earthquakes. Notably, the Tohoku earthquake (M = 9.1, 2011), Wenchuan earthquake (M = 7.9, 2008), Haiti earthquake (M = 7.0, 2010) happened in areas that had been seismically quiescent and were considered low risk [*Stein et al.*, 2012; *Frankel*, 2013].

An alternative and more deterministic approach to assessing seismic risk, particularly in areas that have been historically aseismic, is to evaluate the stability of candidate faults under the framework of the Coulomb friction law. Deterministic susceptibility analysis that does not rely on the study area's past earthquake history is needed. Such analysis provides better insight into understanding the risk of induced earthquakes and allow comparison with statistical susceptibility map for objectivity test [*Stein et al.*, 2011]. The growth of deep waste fluid disposal and large-scale hydraulic fracturing for both geothermal and hydrocarbon resources motivates further development of these direct assessments, particularly in historically aseismic areas.

According to the Coulomb static frictional criterion, slip occurs on a plane of weakness once the in-plane traction exceeds the clamping force that depends on the effective plane-normal traction, a static coefficient of friction, and a cohesive strength [*Jaeger and Cook*, 1976]. Once sliding commences, dynamic rate-state frictional relations may be invoked to describe subsequent behavior [e.g., see review in *Marone,* 1998]. For a study area that has a history of past natural earthquakes, it is probable that earthquakes can occur on planes of weakness that may have already been imperceptibly creeping at extremely small rates. However, for area that is historically aseismic (e.g., this study area), it is not clear that a rate-state formulation, which would require accurate knowledge of actual long-term slip rates and material properties, is warranted. Hence, stability analysis that relies on the static frictional principles originated by *Amontons* [1695; 1699] should suffice. *Amontons* [1695; 1699] first proposed, through a serious of experiments, that the friction provided by a contact surface is proportional to the normal pressure. This observation was further advanced by *Coulomb* [1773]. Within the context of rock mechanics these concepts are supported by *Byerlee's* [1978] later finding that the static frictional coefficient μ, constrained between 0.6 to 0.85, can reasonably describe rock friction. More recently, a meta-analysis provided in *Shen et al.* [2019b] that incorporated results from 15 papers show that the frictional coefficient of shale, with varying quartz and clay content, under constraining pressures of 100-200 MPa, can be reasonably constrained between 0.4 to 0.8; μ = 0.6 remains a simplified, yet reasonable assumption.

Despite this straightforward principle, direct quantitative analysis of the slip-tendency of faults remains rare [e.g., *Schwab et al.*, 2017], largely owing to the difficulties in obtaining reliable quantitative stress magnitudes and fluid pressures; those variables are required to resolve for the traction forces on the fault planes. To date, most fault stability studies are forced to make numerous assumptions to obtain estimates on the stress. These often include reliance on frictional constraints along hypothetical optimally oriented, critically stressed faults [e.g., *Townend and Zoback,* 2000] or application of the lateral constraint concept [e.g., *Eaton*, 1969; 1975]. The estimated values provided by these methods may deviate significantly from the actually values. More accurate stress field information can only be reliably obtained from deep boreholes. Consequently, the state of stress is best constrained by different but complementary measurements, and the economic costs associated with obtaining this information can be prohibitive. If stress field data are available, they should be used as one component of a hazard assessment in areas with low or nonexistent historical seismicity.

Here, we carry out the frictional stability analysis, using the principals described by *Amontons* [1695; 1699] and *Coulomb* [1773], for faults in an area (~200 km × 200km, near the city of Red Deer, Canada, **Figure 1a**) subject to active hydraulic fracturing stimulation of the Duvernay Formation. Importantly, this area has relatively low levels of historical induced seismicity. We start by reviewing the geological stratigraphy and known structure in this area, as well as the history of natural and induced earthquakes regionally. We then constrained, using borehole measurements from different depths within the Duvernay Formation, 3D distribution of the complete stress tensors and formation pore fluid pressures for the volume of crust studied here. These information subsequently allows us to perform a series of fault slip tendency analyses to assist understanding of the factors responsible for inducing slip in the one significant event (Mar

06, 2019, M_W 3.8/M_L 4.2 near Red Deer, hereafter referred to as *Event A*, **Table 1**). These concepts are further extended to construct a seismic susceptibility map over the area. We find that owing to relatively high ambient pore fluid pressures in the target formation, large ranges of possible fault orientations are vulnerable; and small perturbations in pore fluid pressure would easily make these faults unstable. Our analysis of susceptibility reveals a strong correlation with recorded earthquakes, but the susceptibility map does not always corellate with areas where there has been an absence of seiscmicity, for which we provide some interpretations.

Table 1. Significant seismic events in the area and relation to stress field constrained in this study.

			Conjugate plane orientations reported by seismological observation				Constrained Andersonian stress through this study					
								Principal Components (MPa)				
Event	Date M_W	Epicenter Depth	Plane	Strike	Dip	Rake	Azimuth ϕ	S_h	S_V	S_H *(Borehole Failure)*	S_H *(focal mechanism inversion)*	P_P
A*	03/04/2019 M_W 3.8	N52.20° W114.11° 2.5 km	1	101°	72°	-30°	N47°E	46	61	75 – 116	65 -106 (median: 84)	40
			2	201°	62°	-160°						
B*	03/10/2019 M_W 3.9	N52.57° W115.26° 15 km	1	138°	49°	77°	N52°E	-	-	-	-	-
			2	338°	42°	105°						
C†	10/19/1996 M_W 3.4	N52.21° W115.25° 5.2 km	1	205° *156°*	44° *44°*	136°	N50°E	110	132	132 - 155	-	-
			2	329° *302°*	61° *51°*	55°						

*reported in *Schultz and Wang* [2019]

†focal mechanism analysis attributed to *R. Horner* as provided in *Baranova et al.,* [1999].

2 Geological background and induced earthquakes

This section overviews the regional geological framework and its history of natural and induced seismicity. The study focuses on a ~200 km × 200 km study area) that includes the city of Red Deer (see **Figure 1a)**. The study area had seen induced seismicity associated with active hydraulic fracturing operations in the Duvernay Formation.

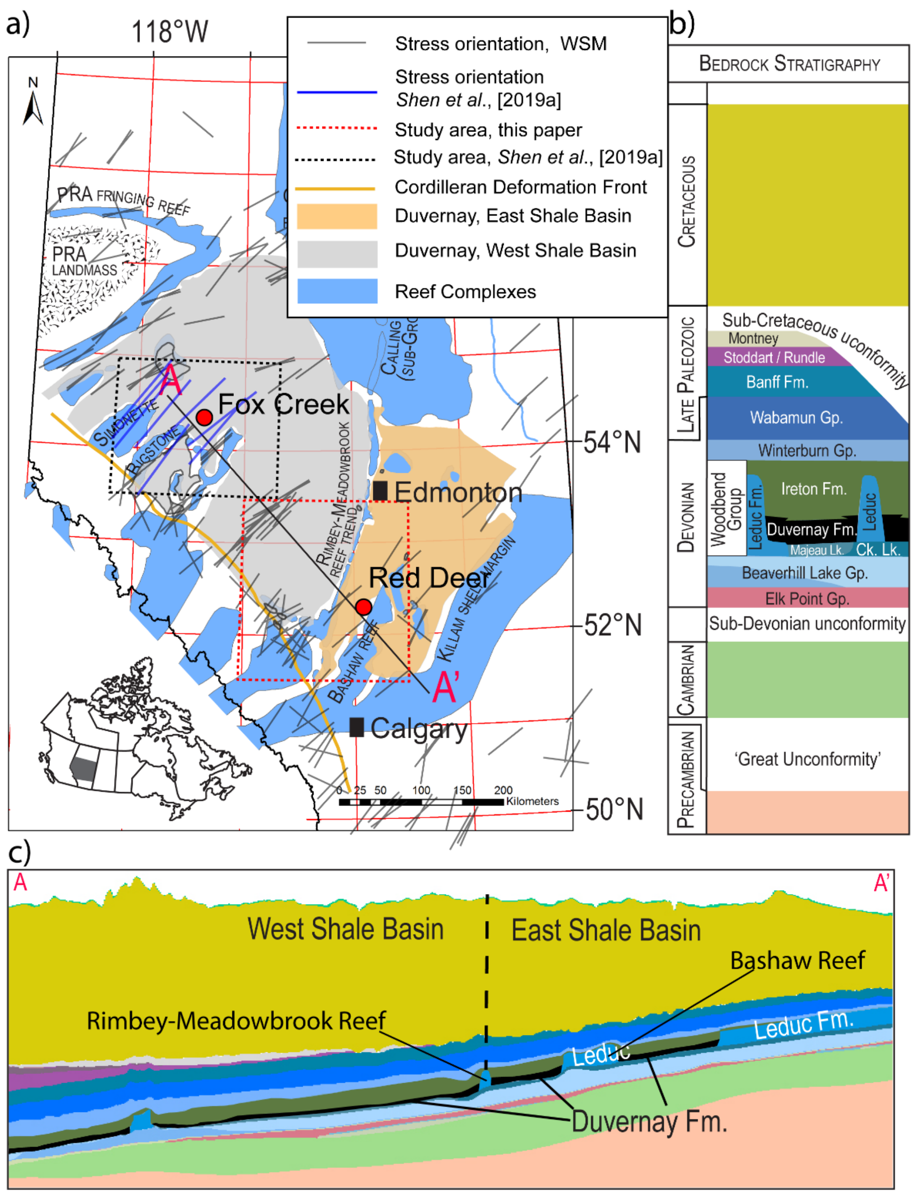

Figure 1. **a)** Overview of the study area in Alberta, Canada with West Shale Basin (WSB) and East Shale Basin (ESB), which contains the Duvernay Formation, separated by the Rimbey-Meadowbrook reef trend.

Gray dashes represent the direction of the maximum compression S_H reported in the World Stress Map. **b)** Bedrock stratigraphy of western central Alberta with elements from the cross-section shown in **c)** for the line A-A' in a). Vertical depth in c) is exaggerated 50 times.

2.1 Regional geology

In the study area, the sedimentary succession forms part of the Western Canada Sedimentary Basin underlain by Paleoproterozoic metamorphic and igneous basement (**Figures 1b, c**). The sedimentary column consists of 1) a thick succession of Paleozoic carbonates, shales, and evaporites deposited predominantly during tectonic quiescence, and 2) an upper succession of Mesozoic basin-filling siliciclastic strata that formed in response to orogenesis along the western margin of North America. Orogenesis initiated in the Late Jurassic (circa 163 Ma) and continued through to the Eocene (52.1 Ma) [*Pană and van der Pluijm*, 2015]. Significant unconformities separate the sedimentary successions from the underlying crystalline rocks and within the sedimentary succession between phases 1 and 2. The Cordilleran Deformation Front is another important structural element (**Figures 1a, 2**) that separates highly deformed sedimentary strata in the SW from undeformed strata of the plains to the NE.

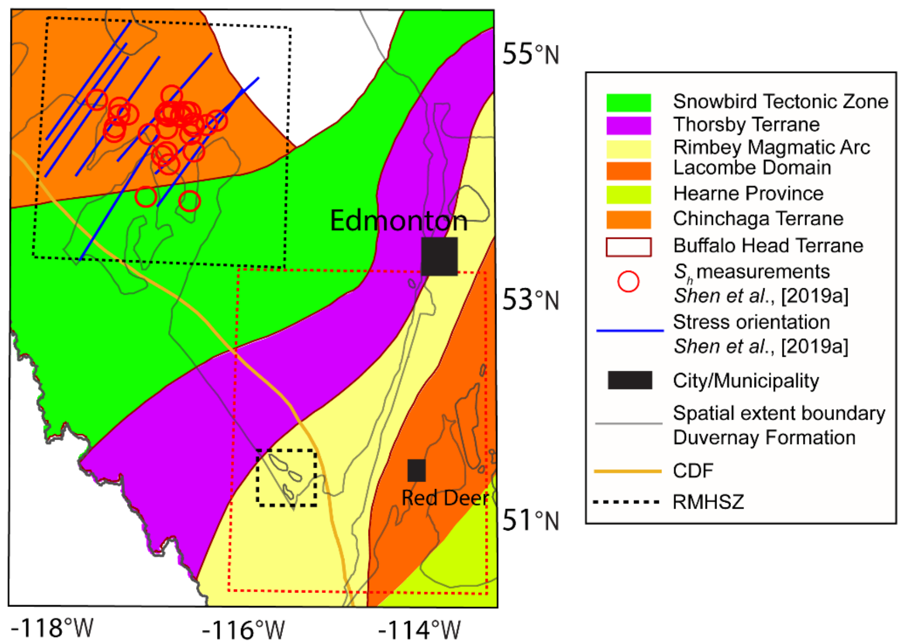

Figure 2. Geological features of our study area associated with the tectonic provinces mapped by *Ross et al.* [1991] with their boundary lines reproduced by *Gu and Shen* [2015]. The Red dashed box denotes our study area that includes the Rocky Mountain Seismic Hazard Zone (small black dash box, RMSHZ). The larger black dashed box to the north is the study areas of *Shen et al.,* [2019a]. Brown solid line represent the Cordilleran Deformation Front (CDF).

The Devonian Duvernay Formation is the target for industrial hydraulic fracturing activites within the study area. The Rimbey-Meadowbrook Reef Trend (**Figures 1a, 3a**) bisectes the Duvernay Formation into the West Shale Basin (WSB) and the East Shale Basin (ESB) [*Preston et al.*, 2016]. The portions of WSB and ESB lying within the study area also fall within the Edson-Willesden Green (WG) and the Innisfail Regulatory Assessment Areas [*Preston et al.*, 2016]. Paleogeographic elements of the ESB include the Bashaw Reef complex that separates the Westerdale and Ghost Pine embayments. The depth of the Duvernay Formation (**Figures 3b**) increases significantly from NE to SW due to structural dip toward the orogenic front and increasing surface topography westward (**Figures 3c**).

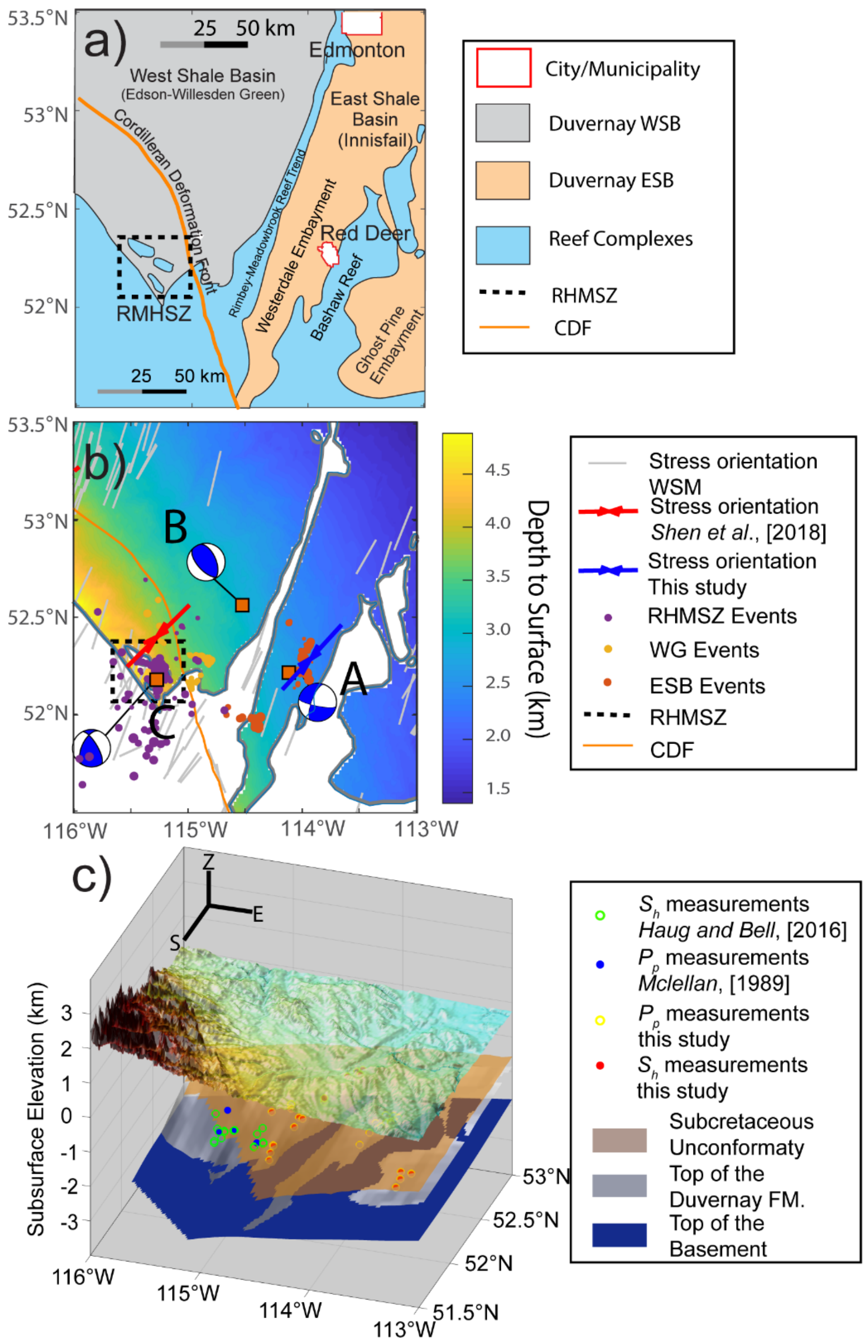

Figure 3. a) Paleogeographic features associated with the Duvernay Formation, including the West Shale Basin (WSB) and the East Shale Basin (ESB). RMHSZ stands for rocky mountain house seismic zone;

CDF stands for cordilleran deformation front. **b)** Detail map of epicenters within the study area, the background color indicates depths from surface to the tops of the Duvernay Formation. Outlined brown squares: three major earthquakes designated A, B, and C with focal mechanism resolved (details Table 1). WSM stands for world stress map. Red arrow shows the measurements reported earlier by *Shen et al*. [2018] and blue arrow shows a measurement newly collected in this work. **c)** 3D view of the study area and locations of stress measurements reported earlier. Model layers include, in stratigraphically descending order, the land surface, sub-Cretaceous unconformity (see **Figure 1**), Duvernay Formation, and Precambrian basement.

Precambrian basement rocks in the WCSB comprise several Archean- to Paleoproterozoic-aged tectonic provinces [*Ross et al.*, 1991; *Ross and Eaton*, 1999, see **Figure 2**]. The Archean portion of the basement represents the oldest and most stable part of the cratonic rocks that make up the core of North America. Younger rocks were welded to the Archean crust in the Paleoproterozoic during accretionary and collisional processes [*Hoffman*, 1988]. The Precambrian tectonic domains within the study area were delineated through potential field maps and U-Pb geochronology from basement samples taken from drill-cores [*Burwash et al.*, 1994; *Ross and Eaton*, 1999; *Ross et al.*, 1991]. A prominent feature in potential field data is the NE-trending Snowbird Tectonic Zone, which bisects the basement in the northwestern part of the study area (see **Figure 2**). LITHOPROBE 2D seismic profiles that cut through the NE section of the study area also contains several notable features: 1. a series of reflectors with an apparent westward dip of about 45° in the uppermost metamorphic crust; 2. a strong subhorizontal reflector interpreted as an abrupt change in metamorphic facies [*Bouzidi et al.*, 2002] or as regional sills at about 15 to 20 km depth; 3. an abrupt 10 km change in the topography of the Mohorovičić discontinuity [*Bouzidi et al.*, 2002] that hints at tectonic activity in the distant past.

Despite the apparent features revealed in the crustal-scale seismic-reflection profiles, there is little clear evidence for any large-scale tectonic reactivation within the Precambrian basement. Nevertheless, numerous studies [see recent review in *Corlett et al.*, 2018] have used various lines of evidence suggesting that the modest fault displacements of the basement may have influenced deposition of Paleozoic strata. If fault-related displacements of the basement exist in the study area, they remain below the limit of seismic resolution [*Ross and Eaton*, 1999]. For example, *Edwards and Brown* [1999] attempted to relate the 540 km long, suspiciously linear Rimbey-Meadowbrook Leduc Reef trend that runs through the study area to possible basement structure, but they were not able to detect such a relationship within the resolution of their reflection seismic data. However, the debate of possible Precambrian basement control on the overlying Phanerozoic sediments is longstanding [see *Moore*, 1988].

The top of the Precambrian basement marks a global event, known as the 'great unconformity' [*Peters and Gaines*, 2012]. The basement (see **Figures 1b, c**) is overlain by Middle Cambrian rocks in turn overlain by Devonian strata, separated by the sub-Devonian unconformity. This Devonian succession comprises 1) a middle Devonian package of mostly siliciclastics and evaporites; 2) an upper Devonian succession of carbonate reefs and intervening basin-filling shales. Within the upper Devonian succession, the Duvernay Formation consists mainly of bioturbated siliceous, calcareous, and argillaceous mudstones. The Duvernay Formation is the main target for HF because of its attractive organic content [*Rokosh et al.*, 2009] and mechanical stiffness. The Duvernay Formation still retains significant gas and condensate hydrocarbons that motivate exploitation with horizontal drilling and associated hydraulic fracturing.

The Devonian succession is overlain by late Paleozoic strata at the top of which is the sub-Cretaceous unconformity (see **Figures 1b, c**). Early Cretaceous siliciclastic sediments lie above this unconformity and were deposited into a flexural foreland basin [*Beamont,* 1981] formed by the crustal loading that was initiated by plate convergences to the west commencing possibly as early as the late Jurassic [*Chen et al.*, 2019; *Pană and van der Pluijm*, 2015]. The flexure of the Precambrian basement surface and the Paleozoic strata is particularly apparent as an increasing structural dip toward the orogen in the west. Sequences of major thrust faults and other complex structures are exposed in the fold and thrust belt southwest of this Cordilleran Deformation Front [e.g., *Price*, 2001].

Structure within the deformed belt contrasts with a relative paucity of known faults in the study area to the east of the Cordilleran Deformation Front. That said, faults are known to exist outside of the study area with evidence from seismic-reflection profiles displaying faults that intersect successions through the Paleozoic to the Mesozoic: both to the north associated with the Peace River Arch [e.g., *Weides et al.*, 2014] and to the south [e.g., *Galloway et al.*, 2018; *Lemieux*, 1999]. In other locales, faults have not been explicitly imaged. However, their existence has been inferred from various attributes [e.g., *Chopra et al.*, 2017; *Corlett et al.*, 2018; *Eaton et al.*, 2018; *Ekpo et al.*, 2017; *Weir et al.*, 2018]. Sedimentation patterns and accommodation trends within the basin could also be indicative of differential vertical displacements. For example, to the north of our study area, syndepositional motion along faults related to the Snowbird Tectonic Zone may have resulted in anomalous localized thickening of the Albian Viking Formation [*Schultz et al.*, 2019].

2.2 Regional seismicity: natural and induced

This study area has historically experienced low levels of seismicity. Only 35 cataloged events above M_W 2.5 since 1960 [*USGS*, 2020] are reported. Most of these are associated with a cluster occurring in the SW part of the study area, possibly related to natural gas production during the 1980s, in a region consequently referred to as the Rocky Mountain House Seismic Zone (RMHSZ) [*Rebollar et al.*, 1982; *Wetmiller*, 1986, **Figures 2, 3a, 3b**]. However, it is important to note that the RMHSZ lies within the deformed zone to the SW of the Cordilleran Deformation Front. The 1996 *Event C* (see **Table 1**) from this sequence is included in Table 1 for comparison.

Since 2010, HF activities targeting the Duvernay unconventional reservoir have been linked to induced earthquakes. Most of these events are located near the town of Fox Creek north of the current study area, where a series of $2.5 < M_L < 4.7$ earthquakes, including some felt by the local residents, triggered the *Alberta Energy Regulator*'s [2015] traffic light protocol for ceasing operations.

In contrast, the southern sections of the Duvernay Formation of the current study have been largely seismically quiescent; and consequently were assessed with low seismic risk [*Pawley et al.*, 2018]. The differences in the levels of seismicity between the northern Fox Creek and the southern current study area, despite similar concentrations of HF activity since 2012 [*BMO*, 2019], provided the initial motivation for this work. This seismic quiescence ended with two events occurring near the city of Red Deer that were felt by the residents. The first in March 2018 followed by a larger event in March 2019 (*Event A*, see **Table 1** and **Figure 3b**). Immediately after *Event A*, *Alberta Energy Regulator* [2019] ordered the shut-in of the responsible seismogenic wells [*Schultz and Wang*, 2020]. These events accelerated the need for more detailed geomechanical analysis.

The source parameters of the first March 2018 (M_L 3.1) earthquake are poorly constrained owing to the sparse seismometers network near the epicenter at the time [*Schultz et al.*, 2015]. However, a denser recording array was in place to capture the larger *Event A* in March 2019 [*Schultz and Wang*, 2020], allowing for more accurate determinations of its focal mechanism.

Subsequent studies further detected > 1200 additional earthquakes in the Westerdale Embayment from 2014 to 2019 with magnitudes of M_L -0.7 to 4.3 [*Schultz and Wang*, 2020]. These earthquakes are highly correlated, both spatially and temporally, with HF activities in the ESB that commenced in 2012 [*BMO*, 2019]. At the same time, however, no notable induced events have occurred in other sectors of the study area to the north of the city of Red Deer, within the Ghost Pine Embayment, or over most of the Edson-Williston Green zone (see **Figure 3b**).

It is also important to note the occurrence of an M_W 3.9 (M_L 4.3) earthquake (*Event B*) at a depth of 15 km in the NW corner of the study area on Mar 10, 2019 (see **Table 1** and **Figure 3b**). This mid-crustal depth event, its reverse fault focal mechanism, and its distances to any HF activity indicate that it is a natural earthquake [*Schultz and Wang*, 2020]. We included this information in **Table 1** for comparison.

2.3 Earlier reports on the states of stress in the Western Canada Sedimentary Basin

The pioneering studies that related the azimuths of borehole breakouts to stress directions used oriented-caliper log data some of which was obtained within the study area [e.g., *Bell and Gough*, 1979]. These original data reside in the latest version of the Word Stress Map [WSM, *Heidbach et al.*, 2016] and is also part of *Haug and Bell's* [2016] compilation and were reviewed by *Reiter et al.* [2014]. *Shen et al.* [2018] recently added 20 additional measurements from newly analyzed borehole image logs. These studies generally show a relatively uniform NE-SW compression across the Alberta Basin; thus, the azimuth ϕ of the maximum horizontal stress S_H is expected to be ~N45°E in our study area.

Before proceeding further, it is important to mention that within the petroleum industry, the in-situ magnitudes of stress or pore fluid pressures are often reported as 'gradients,' which are simply the actual value divided by the depth of the measurement. For this reason, we refer to it as the 'secant' gradient. The origin of this likely derives from the terminology 'fracture gradient' [e.g., *Eaton*, 1959] that is the fracture pressure, which is the pressure needed to hydraulicly open a fracture, divided by the total vertical depth. This fracture pressure-to-depth ratio (fracture gradient) allows engineers to perform quick estimates of the drilling fluid density to balance the needs of maintaining wellbore stability and preventing blowout versus avoiding loss of circulations through inadvertent hydraulic fracturing due to the fluid column pressure alone. While this is useful for making engineering design decisions, it does not necessarily allow for more accurate prediction of stress.

Here, the ensemble of borehole observations allows us to collect numerous S_h and P_P within the Duvernay Formation over a range of depths. The slope of the line obtained by simple linear regression of these values versus the depth is referred to as the tangent gradient following *Shen et al.*, [2018, 2019a, b]. The predictive formula (presented later) uses linear regressions of actual measurements within the Duvernay Formation to provide more accurate predictions of pore pressure and stress. Essentially, this 'tangent' gradient allows for the effect of the variable depths of the Duvernay Formation to be accounted for in the construction of the maps of S_h and P_P. Strictly, these values should only apply to measurements within the Duvernay Formation itself.

S_h magnitudes can be measured directly in certain transient pressure tests by finding the pressure P_{fc} at which a small induced hydraulic fracture closes during pressure decline. These tests are variously referred to as extended leak-off tests, micro-fracture tests, mini-fractures tests, or diagnostic fracture injection test (DFIT™); the detailed methods used in the analysis of such records are reviewed by *Shen et al.* [2018]. Within the basin, there are over 100 previously reported S_h measurements through a series of studies [*Bell and Caillet*, 1994; *Bell and Bachu*, 2003; *Bell and Grasby*, 2012; *McLellan*, 1989; *Woodland and Bell*, 1989; *Haug and Bell*, 2016] from which

McLellan [1989] calculated an average secant gradient of 19 MP/km. These compilations include 39 values of S_h and 16 values of P_P lying within the current study area (**Figure 3c**). However, all of these measurements were made in the younger Mezosoic formations, and many of them from actively producing oil/gas fields. These values may deviate from the undisturbed virgin states. Herein, these measurements are displayed later for the sake of comparison. However, we do not include them in developing our predictive formulas for stress states of the Duvernay Formation that are later applied to fault stability calculations.

The unconventional Duvernay Formation had not been considered a viable reservoir before the mass adoption of the HF technique, and we are not aware of any Duvernay stress measurements before 2010. *Shen et al.* [2018] recently provided 38 values of S_h and P_P by analyzing pressure records obtained since HF operations in the Duvernay Formation commenced, 12 of which lie within the current study area. These are incorporated with the new measurements described below in the construction of the stress distribution model.

No reliable method to directly measure S_H magnitudes from deep boreholes yet exists; it can only be constrained. *Shen et al.* [2019a] attempted to overcome this limitation in the Fox Creek area by combining the measured values of S_h, S_V with the 'shape factor *R*' [*Bott*, 1959] derived by inverting the local focal mechanism to provide constrained S_H distribution; efforts had also been made with borehole failures identified by examining the image logs [*Shen et al.*, 2018]. These inversions, also show σ_2 is close to vertical in agreement with the Andersonian assumptions, and indicate a strike-slip faulting environment within the Duvernay Formation.

3 Stress measurements and fault stability

3.1 Data and Quantitative 3D Stress Distribution Model

Here, we develop a model that quantitatively predicts the states of stress for a crustal volume that encompasses the Duvernay Formation within the study area. We would like to reinforce that this is not to be confused with numerical mechanical earth models that attempt to dynamically calculate stresses and pore pressures based on assumptions about structure, physical properties, boundary conditions, and external loads [e.g., *Baranova et al*., 1999; *Deng et al*., 2016; *Hui et al*., 2021]. While this approach is now popular, it does suffer in that numerous assumptions must be employed in constructing the structure, populating it with appropriate physical properties, assigning magnitudes of matrix and fracture transmissivities, and applying correct loads. A lack of such data lead us to instead expend efforts in understanding as best possible the stress tensor and pore fluid pressures based on numerous borehole observations. In the end, we provide a Matlab™ program RD_stress.m [*Shen and Schmitt*, 2020] that allows users to estimate the stress magnitudes within the Duvernay Formation as a function of latitude, longitude, and depth.

The conventions used here assumes an *Andersonian* [1951] stress tensor with a vertical S_V compression, maximum S_H, and minimum S_h horizontal stress completed by the azimuth ϕ of S_H [e.g., *Schmitt et al.*, 2012; *Shen et al*., 2019a]. In the context of a strike-slip stress regime, the three principal compressions are σ_1 (=S_H) > σ_2 (=S_V) > σ_3 (=S_h). Further determination of the formation rock's pore fluid pressure P_P is necessary for calculating effective stresses and understanding potential rock failure. Following common geomechanical convention, fluid pressures and compressive stresses have positive signs. Analyses on S_h, S_V, P_P, and ϕ employ methods similar to those used the earlier studies of the Fox Creek area [*Shen et al.*, 2018; 2019a]. Here, only a brief summary of the results is provided.

3.1.1 Stress direction Azimuth ϕ

A grid of stress orientations ϕ, defined as the clockwise rotational angle between the geographic north and the direction of S_H (**Figure 4a**), is developed from the interpolation of a set of observed breakouts and drilling-induced fractures that incorporates orientations from one newly analyzed image (Lat: 52.3, Lon: -114.0, see **Figures 3b**, **4a**) near the city of Red Deer with the 54 earlier determinations in published compilations [*Reiter et al.*, 2014; *Haug and Bell, 2016; Shen et al.*, 2018] many of which are in the World Stress Map (WSM). We observe no correlations between ϕ and depth, in agreement with our earlier study to the north [*Shen et al.*, 2019a]. The program RD_stress.m provides a value for ϕ on the basis of the latitude and longitude by interpolation within the stored matrix of $\phi(x,y)$. This matrix itself is a weighted interpolation of the observed orientations using procedures described in detail previously [*Shen et al*., 2019a]. Owing to a paucity of natural fractures in the image logs available to us, we are unable to employ recently developed methods that employ natural fracture orientations [e.g., *Ameen*, 2019].

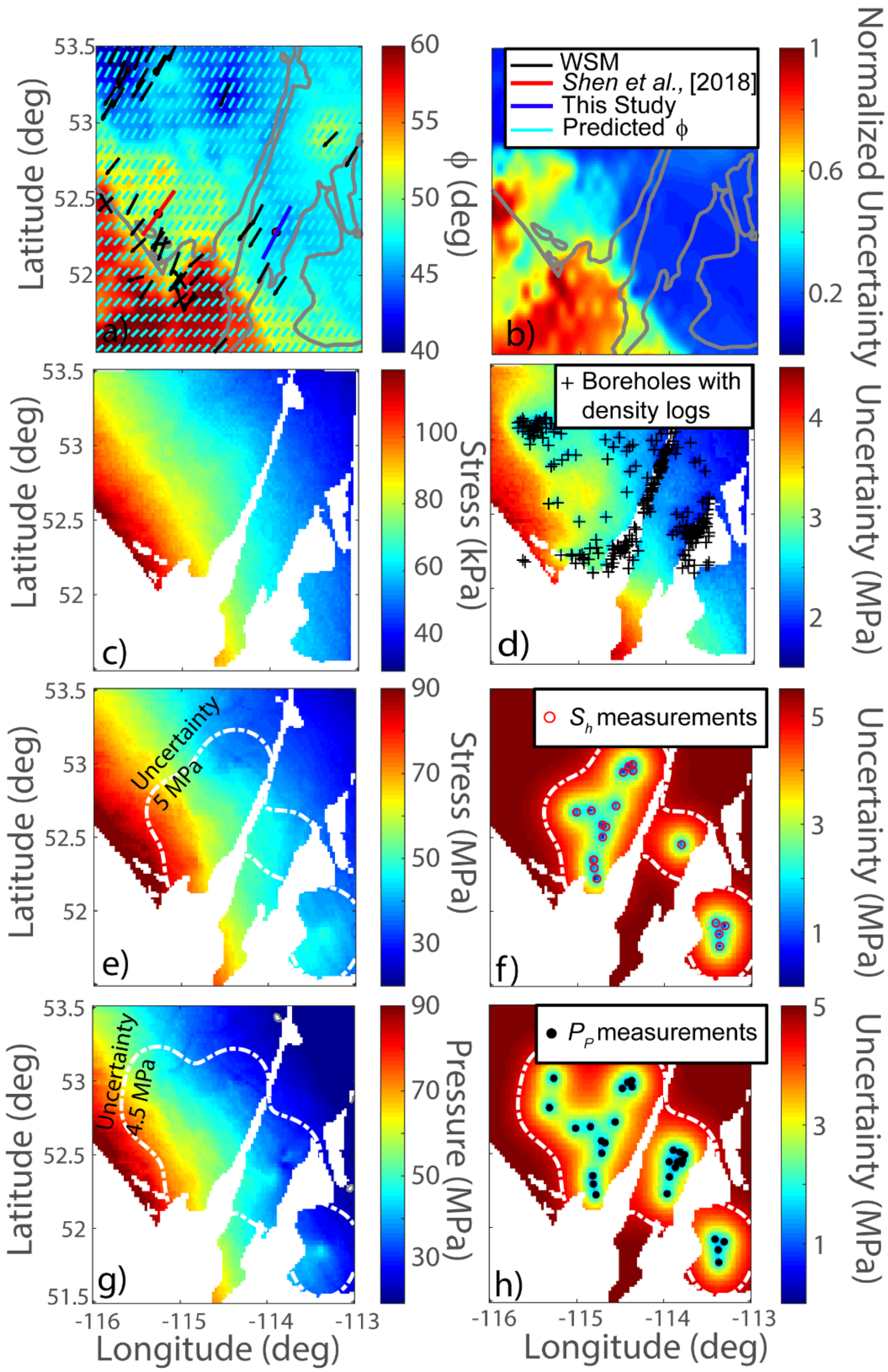

Figure 4. Spatial maps for the states of stress in the mid-point of the Duvernay Formation of our study area. **a)** Orientation of S_H and **b)** normalized uncertainty (from 0 - 1). **c)** Magnitudes of S_V and **d)** uncertainty. **e)** Magnitudes of S_h and **f)** the uncertainties. **g)** and **h)** show the P_P and the uncertainties. White contours in e) to h) show the enclosed areas with uncertainties of less than 5 MPa for S_h and 4.5 MPa for P_P.

We provide a normalized uncertainty in $\phi(x,y)$, which ranges from 0 to 1 (**Figure 4b**). This metric depends on both the distance of a given location (x,y) to nearby observations and an assessment of each measurement's quality. The normalized uncertainty approaches 0 if the prediction is made with at least three nearby measurements with high consistency. On the other hand, uncertainty approaches 1 for locations that are either far away from observations and/or with multiple observations, nearby, reporting different ϕ (e.g., the southwest corner of **Figure 4a**). In general, uncertainty on the predicted stress orientation ϕ in the southwest of our study area is higher where Leduc Reefs grew contemporaneously with the Duvernay Formation. Such large uncertainties arise from large variation of WSM observations within limited region (see Figure 4a).

3.1.2 Vertical Stress S_V,

The vertical stress S_V at the depth of the Duvernay Formation (**Figure 4c**) and its uncertainty (**Figure 4d**) is obtained first by integrating 681 density logs (see **Figure 4d**), combining these into a 3D volume, and then correcting for variations in topography using a Green's function method [*Liu and Zoback*, 1992], with procedures detailed in *Shen et al.* [2019a]. This Green's function method essentially applies a low-pass filter that removes the influences of short-wavelength topographic changes (e.g., valleys and hills) while preserving longer wave-length regional trends that impact S_V at greater depth. We avoid using a simple gradient to estimate S_V due to the complications that arise from 1). the lateral and vertical variations in the structure, 2) the density differences between siliciclastics and carbonates typifying the rock masses above and below the sub-Cretaceous unconformity.

3.1.3 Least Horizontal Compressive Stress S_h magnitude and pore fluid pressure P_P

We combine 8 new determinations of Duvernay S_h magnitudes to the 12 in the database mentioned above [*Shen et al.* 2018]. Linear regression of these plotted as a function of depth z to the mid-point of the Duvernay Formation (**Figure 5a**) yields

$$S_h(z) = (22.2 \pm 5.6 \frac{MPa}{km})z - (12.8 \pm 3.4)\ MPa \quad (1)$$

Similarly, 20 new determinations of pore fluid pressures P_P, added to the 22 results from the *Shen et al.* [2018] database give the expression used to estimate pore pressure (**Figure 5b**)

$$P_P(z) = (24.8 \pm 3.6 \frac{MPa}{km})z - (23.8 \pm 10.0)\ MPa \quad (2).$$

All of the available local Mesozoic determinations of S_h and P_P [*Haug and Bell*, 2016; *McLellan*, 1989] are also displayed in **Figure 5**, but only for the sake of comparison; these data are not included in **Eqns. 1** and **2**. The 'tangent' gradiens employed later are simply the slopes of **Eqns. 1** and **2**.

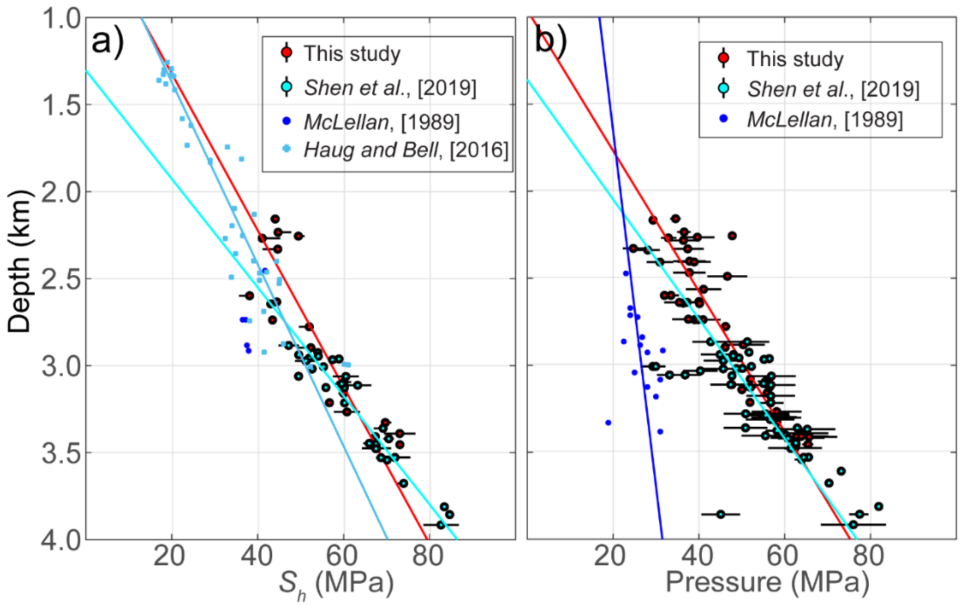

Figure 5. Reported measurements (with their respective uncertainties) and linear regression results for **a)** S_h magnitude and **b)** P_P from different sources. In **a)** the cyan line shows the linear regression of the

measurements of *Shen et al*. [2019a]; the teal line represents the linear regression of *Haug and Bell* [2016] data. The red line denotes the linear regression of the data utilized in this work. In b) the blue line denotes the linear regression of pore pressure data from *McLellan* [1989]; cyan and red lines show the linear regression of *Shen et al*. [2019a] measurements and data utilized in this work.

The S_h (**Figure 4e**) and P_P (**Figure 4g**) are those predicted at the top of the Duvernay Formation using the methods in *Shen et al*. [2019a], with the corresponding uncertainty mapped in **Figures 4f, h**. In short, we shifted each of the measured S_h and P_p to the different depths using the tangent gradients $\Delta S_h(z)/\Delta z$ and $\Delta P_P(z)/\Delta z$ (Eqn. 1 and 2). Accordingly, the uncertainties are updated with error propagation. Subsequently, simple kriging is performed with measurement points shifted into the same depth level, with the uncertainty of the prediction calculated as the square root of the kriging variance. The uncertainties shown are governed by two factors: 1) the uncertainties of the measurements as assigned during the reinterpretation of the pressure records [see *Shen et al.,* 2018, for details] and 2) the proximity of the actual measured values to the location at which a value is desired. The uncertainty increases with distance from actual measurement locations, and at sufficient distance, essentially collapses to the observational variances. Consequently, the S_h and P_P uncertainties generally range lows of 0.5 to 1 MPa and rise to 5.0 to 5.5 MPa further away. Generally, we consider the values predicted within the white contours in **Figures 4e - h** delimiting uncertainties of 5 MPa for S_h and 4.5 MPa for P_P to indicate reliable estimates. Users can use RD_stress.m to obtain S_h and P_P as functions of latitude, longitude and depth.

3.1.4 Constraints on the magnitude of S_H

Given the uncertainties associated with the quantitative determination of S_H we attempt to obtain representative values three ways: 1) frictional constraints under the critically stressed crust paradigm, 2) interpretation and extrapolation of borehole failures observed in image logs, and 3) shape factor inversion of the observed focal mechanism for *Event A*. All these estimates require prior knowledge of S_h, as detailed above. In this work, we constrain S_H mainly through methods 2 (**Figure 6a**) and 3 (**Figure 7**).

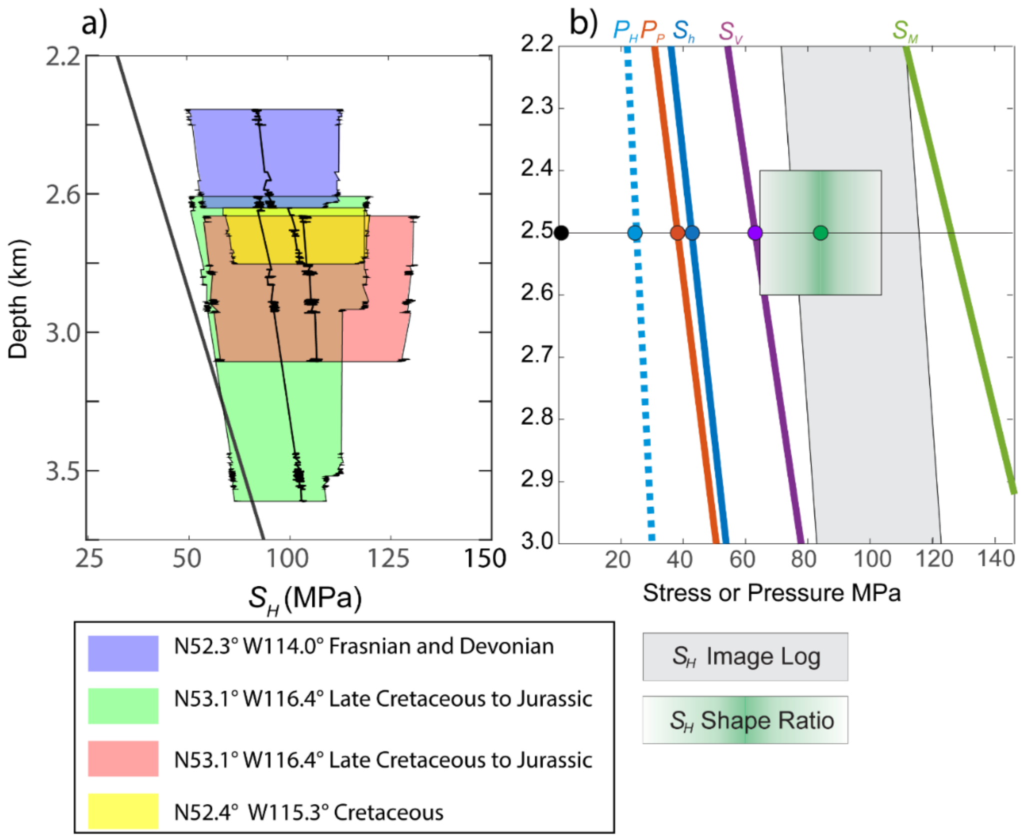

Figure 6. a) Estimated maximum stress S_H from borehole breakouts. The width of the polygons mark the 25th to 75th percentile of the cumulative probability density functions for S_H constrained through borehole breakouts, computed using Monte-Carlo methods, and the black lines stand for median values of S_H. The black straight line represents the estimated S_V assuming a linear relationship with depth of $S_V(z)$= z×25.5 MPa/km. b) Comparison of P_H (dashed blue line, hydrostatic pressure), P_P predicted by data derived Eqn. 2 (orange line), S_h predicted by data derived Eqn.1 (blue line), the linear S_V (purple line), and different constraints on S_H. The green line denotes the upper bound estimated with the strength of optimally oriented fault S_M, (Eqn. 3, with $\mu = 0.6$). The gray-filled zone represents the range from breakouts. The distribution from inversion of the focal mechanism of **Figure 7b** is shown as the green shaded box. Colored dots mark

the estimated hypocentral depth of *Event A* showing corresponding values used in fault stability calculations.

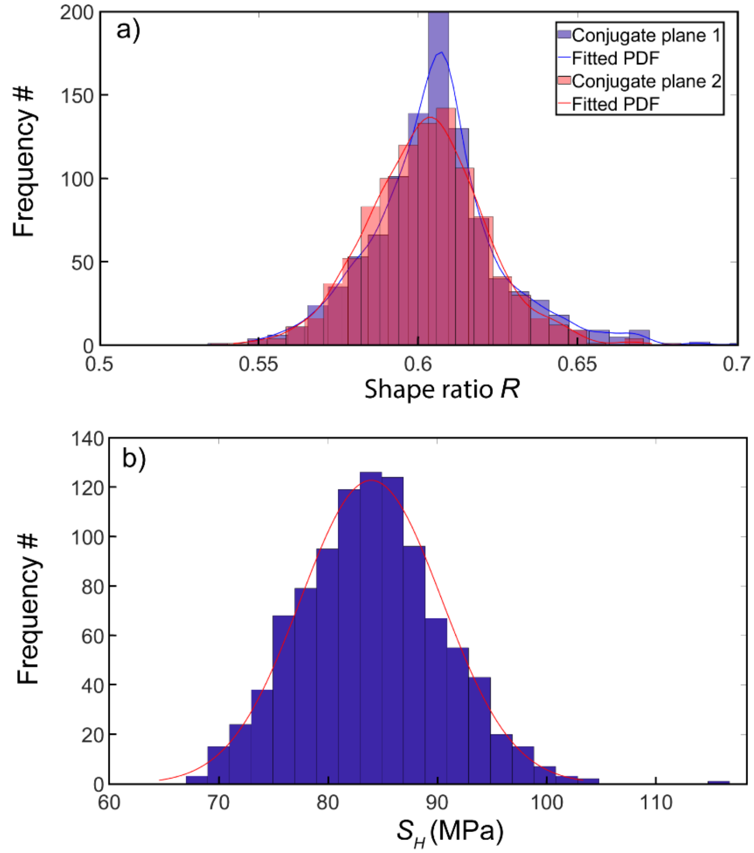

Figure 7. a) The distribution of shape factor R computed for both conjugate fault planes from the earthquake's (M_W 3.8/M_L 4.2) focal mechanism. **b)** Inverted S_H with the predicted S_h and S_V at the epicenter, using the R distribution from conjugate Plane 1, assuming an Andersonian strike-slip stress regime.

Constraining S_H magnitude through extremum critical slip

The most straightforward critically stressed crust constraint presumes that optimally oriented planes of weakness are always present. The stability of these planes, further modulated by friction and pore fluid pressure, controls the stress levels attainable [*Zoback*, 2010]. In a strike-slip faulting environment, the limiting maximum horizontal stress magnitude, here designated as S_M, is

$$S_M = \left(S_h - P_f\right)\left[(\mu^2 + 1)^{1/2} + \mu\right]^2 + P_f. \tag{3}$$

where μ is the coefficient of friction on the plane of weakness. The largest possible value of S_M is obtained when $P_f = 0$. The trend of this limiting value S_M through the Duvernay Formation, as calculated with S_h predicted by Eqn. 1 and assuming $\mu = 0.6$, is shown for the sake of comparison in **Figure 6b**. However, it is important to reiterate that if there are not optimally aligned planes of weakness, S_H may indeed be larger. Notably, *Shen et al.* [2019b] reported non-optimal alignment of the observed focal mechanisms with the measured stress field for earthquakes in the Fox Creek areas to the north. Varying μ does not mitigate this deficiency.

Constraining S_H magnitude through borehole observation

Analysis of the angular widths β of borehole breakouts provides a second means to constrain S_H. An assumption that the breakouts (BO) result from shear failure on the borehole wall once the rock shear strength is exceeded leads to [*Valley and Evans*, 2019]

$$S_H = \frac{C_o + \frac{2P_W}{1-sin\psi} - \frac{2P_P sin\psi}{1-sin\psi} - S_h(1-2\cos\beta)}{1+2\cos\beta}, \tag{4}$$

where $\psi = \tan^{-1}(\mu)$ is the internal friction angle for the intact rock, C_0 is the unconfined compressive strength, and P_w is the wellbore fluid (mud) pressure. If $P_P = P_w$, this collapses to a form that excludes ψ

$$S_H = \frac{C_o + 2P_P - S_h(1-2\cos\beta)}{1+2\cos\beta} \tag{5}$$

which, to account for the excess fluid pressure when P_P is different from P_W, matches the values given in the widely used form

$$S_H = \frac{C_o + 2P_P + \Delta P - S_h(1 - 2\cos\beta)}{1 + 2\cos\beta} \tag{6}$$

that $\Delta P = P_w - P_P$ [*Barton et al.*, 1988]; this equation only applies when P_w is close to P_P. Eqn. 6 estimates S_H assuming the P_w is reasonably close to P_P [*Barton et al.*, 1988]. In practice, the validity of this assumption is challenged by several factors, mostly revolving around the pressure difference between the P_P and P_w.

Here, we analyzed the borehole images that had also provided constraints on the stress orientation. Due to the limited available data, we also included two more sets of borehole images from locations slightly to the west of our study area. It is also important to note that many of the observations arise from BO in other geological formations. Three of the image logs analyzed in this study report the segments of borehole BOs observed in the Mesozoic formations from the Cretaceous Glauconite to Cardium formations (see **Figure 6a**), with a reported P_P of ~24.6 MPa at 2.6 km (expected $P_w \approx 30$ MPa) to ~28.6 MPa at 3.9 km (expected $P_w \approx 47$ MPa) [*McLellan*, 1989]. From the segments of BOs within the Woodbend Group, including the Duvernay Formation, we observed a P_P of 38.2 MPa (2.5 km deep, expected $P_W \approx 30$ MPa). It is also important to acknowledge the caveats that the reported P_P from *McLellan* [1989] may not represent the virgin state of the reservoir as those measurements were made after extended periods of production. We also do not have knowledge of the P_P in the Ireton Formation (see **Figures 1b, c**) shales overlying the Duvernay Formation.

We analyzed the BO only if two failure features were clearly visible at 180° azimuths. We assigned considerable uncertainty (±10°) to the observed β even for the most visible BO. For shorter or less distinct BOs, which the widths are difficult to determine and thus not reported, a range of 0 - 45° is assumed. Based on laboratory measurements [*Ong et al.*, 2015], this analysis used C_0 from 60 to 160 MPa.

Due to the sparsity of the measurement points and large uncertainties, the construction of regional maps for S_H is impossible. Instead, a vertical profile of S_H is developed. Given the relatively high uncertainties associated with this method, we utilized a Monte Carlo (n = 5000) style analysis using randomly selected input parameters for Eqn. 6 and their corresponding uncertainties of: 1) S_h predicted by Eqn. 1; 2) P_W obtained from wells' drilling reports [see *Shen and Schmitt*, 2020]; 3) P_P predicted by Eqn. 2 for the Duvernay Formation and other geological units by *McLellan* [1989]; 4) ranges of C_0 and β discussed in the paragraph above. A uniform distribution is assumed within the ranges of uncertainties. The median, 25^{th}, and 75^{th} percentiles of the cumulative density function of the calculated S_H distribution are shown in **Figure 6a**. Despite the significant uncertainties inherent to this method, the constrained ranges of S_H are consistent with a strike-slip faulting environment.

Regardless, the constraints obtained through both borehole stability analysis, using observations from the overpressured Duvernay Formation and less pressured Cretaceous -Jurassic geological units, reports that S_H constrained roughly as a function of depth:

$$14.3\frac{MPa}{km}\,z + 40\,MPa \leq S_H(z) \leq 14.3\,\frac{MPa}{km}z + 80MPa \qquad (7)$$

for z (depth) ranges between 2.2 and 3.4 km.

Constrainting S_H magnitude through shape factor inversion

A final alternative S_H constraint relies on the inversion of the focal mechanism for the relative stress magnitudes that are represented by the shape factor R, combined with knowledge of the other two stress tensor components. Assuming that the fault slip parallels the shear traction resolved onto the fault plane [*Wallace*, 1951]; this allows for earthquake focal mechanism orientations to inverted [*Michael*, 1984; *Vavryčuk*, 2014] for the relative deviatoric components of the stress tensor as expressed through the shape factor R :

$$R = \frac{\sigma_1 - \sigma_2}{\sigma_1 - \sigma_3} \tag{8}$$

With a given R, in a strike-slip faulting environment, S_H (σ_1) may be calculated if S_V (σ_2) and S_h (σ_3) are independently known [e.g., *Hardebeck and Hauksson*, 2001; *Shen et al.*, 2019a].

However, one well-known complication is that the focal mechanism solution for an arbitrary earthquake yields two possible conjugate slip planes: a true and an auxiliary fault plane. The true fault plane cannot be found without additional information. There numerous strategies can be employed to determine which plane is preferred [e.g., *Vavryčuk*, 2014]. As we do not know a priori which of *Event A's* planes actually slipped, we carry out separate determinations of R for each.

Here, the *Event A* (see **Table 1**) focal mechanisms is used to determine R. This was accomplished by individually inverting each of the conjugate planes using modified inversion subroutines by *Vavryčuk* [2014]. The distribution of possible R values (**Figure 7a**) was calculated in a 1000-realization Monte-Carlo approach. The strike, dip, and rake of each conjugate plane (see **Table 1**) randomly varied by up to ±5° to account for expected uncertainties in the focal mechanism.

The direct stress inversion performed on both planes both peak at similar shape ratios (0.621 for Plane 1 and 0.608 for Plane 2); adding ranges of uncertainty to the focal mechanism orientations (**Table 1**) produces similar distributions of R between 0.55 and 0.67 (median 0.62, **Figure 7a**).

These R distributions are then combined via the rearranged Eqn. 8

$$S_H = \frac{S_V - RS_h}{1-R} \quad (9)$$

in a second ensemble of Monte Carlo calculations using the determined ranges of 40.3 MPa $\leq S_h \leq$ 50.9 MPa and 58.0 MPa $\leq S_V \leq$ 63.4 MPa from Eqns. 1 and 2, respectively, at the depth of 2.5 for *Event A*. This resulting S_H distribution (**Figure 7b)** has a median value of 84 MPa and ranges across 65 MPa $\leq S_H \leq$ 106 MPa. Using stress inversion results from either conjugate plane does not change the distributions of S_H significantly. S_H constrained through this approach is consistent with that S_H of 75–116 MPa (see **Figure 6b**) constrained from borehole failures.

3.2 Stability analysis for the M_W 3.8 earthquake (Event A)

As noted earlier, the stability or slip-tendency of an arbitrarily oriented plane of weakness [e.g., *Morris et al*., 1996] is governed by the Coulomb frictional criterion that can be assessed by resolving the stress tensor into its effective component tractions normal ($\sigma - P_f$) and tangential (τ) to the plane of interest [see *Schmitt*, 2014, for a review]. Adapting the criterion of *Morris et al.* [1996], slip is expected once the friction on the surface is overcome

$$\mu < \frac{\tau - C}{\sigma - P_f} \equiv SNR \quad (10)$$

In Eqn. 10, we retain the cohesion C, which most authors dispense with, but as shown in *Shen et al.* [2019b], it does noticeably influence the slip-tendency of the plane of weakness. Note this C is different from the rock's UCS denoted as C_0 in Eqns 4-6. Also, in this simplified form, a static frictional coefficient μ controls the ratio between shear friction and normal traction acting on the surface. P_f should be considered the fluid pressure active at the plane of weakness where slip occurs, contrary to the fact that it is omitted in many studies. For reasons discussed later, it is also important to distinguish it from the ambient pore pressure P_P measured from boreholes within the Duvernay Formation [see *Shen et al.*, 2019b]. Admittedly, this simple friction law may not adequately describe the rock's in-situ frictional behavior, particularly in a sense that the friction is impacted by the slip rate [e.g., *Marone*, 1998]. However, in this study, we only attempt to investigate the incipient activation of the fault, and we expect the slip rate is close to zero at this stage. Regardless, no information that is essential to describe a rate-dependent friction law is available for the studied geological units.

We assess the ranges of fault *SNR* at *Event A's* focus by calculating the normal σ and shear τ tractions resolved onto all possible planes [*Shen et al.* 2019b] using the predicted stress states (**Table 1**) with the most probable S_H magnitude (84 MPa). Each *SNR* calculated is plotted in **Figure 8** at the intersection of its planes' pole to its stereographic hemisphere. The calculations are repeated with three different P_f of 1) absent $P_f = 0$ (**Figure 8a**), 2) $P_f = P_H$ of the normal hydrostatic pressure assuming a standard water pressure gradient of 10 MPa/km (**Figure 8b**), and 3) $P_f = P_P$ (**Figure 8c**) as found in our estimate interpolated from the transient borehole fluid tests in the Duvernay Formation. A previous meta-analysis of laboratory frictional measurements [*Shen et al.*, 2019b] suggested friction ranged $0.4 < \mu < 0.8$; these bounding values are shown for the sake of reference as contours in **Figure 8**. Although we do not know the actual frictional coefficients acting at *Event* A's focus, this is taken to be a reasonable range to assess stability. For example, one might expect that those planes subject to *SNR* < 0.4 will remain clamped while those with *SNR* > 0.8 will be increasingly prone to slip [*Shen et al.,* 2019b]. As such, **Figure 8** demonstrates how P_f controls fault stability.

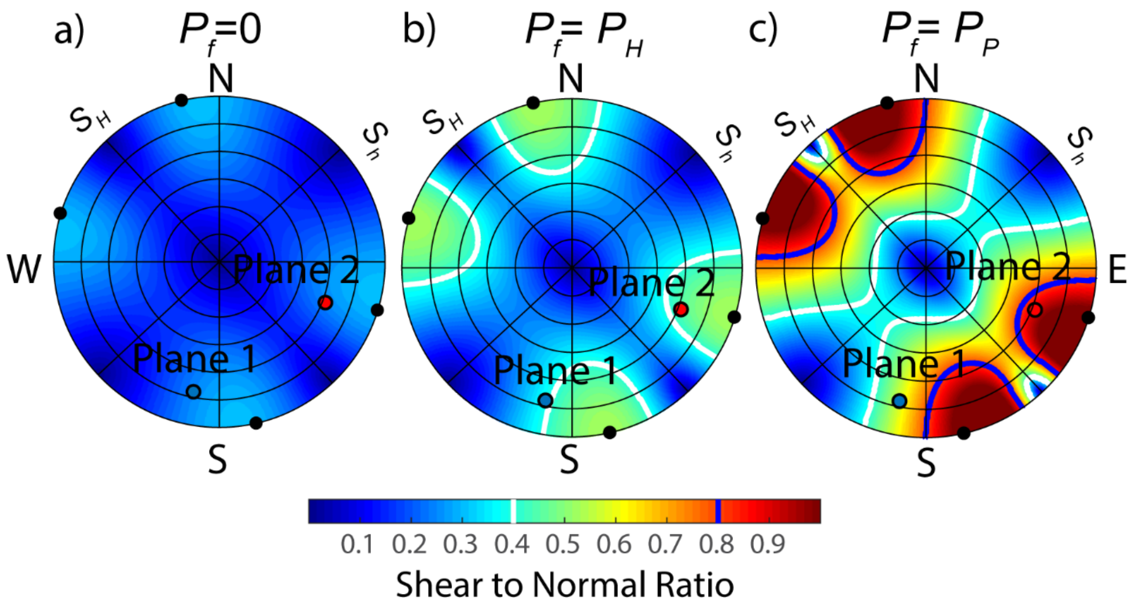

Figure 8. Stereonets of the shear-to-normal ratio (*SNR*) on all possible planes at *Event* A*'s* focus calculated assuming vanishing cohesion *C* with a) no fluid pressure $P_f = 0$, b) normal hydrostatic pressure $P_f = P_H$, and c) Duvernay Formation pore pressure $P_f = P_P$. Blue and red dots are the poles of the two conjugate planes of the event's focal mechanism. Black dots indicate the poles of the optimally oriented fault for slipping.

The stereographic projections of **Figure 8** show the results for three different fluid pressure magnitudes, including the uncertainties of the pressures and frictions. This approach allows for a broader range of possible stability conditions and more stochastic analysis. This approach is widely employed to assess the risk of seismicity through various derived metrics [e.g., *Seithel et al.*, 2019; *Shen et al.*, 2019b; *Walsh and Zoback*, 2016; *Yaghoubi et al.*, 2020]. To better explore these relationships, the critical values of P_f^c required to induce slip [e.g., *Mukuhira et al.*, 2017; *Streit and Hillis*, 2004]

$$P_f^c = \frac{\mu\sigma - \tau + C}{\mu} \tag{11}$$

are calculated separately on each of *Event* A's conjugate planes in a Monte Carlo simulation with 5000 *SNR* realizations that used values of friction $0.4 < \mu < 0.8$, of cohesion $0 < C < 5$ MPa, and ranges of the three principal stresses (**Table 1**). Each of the variables described above is allowed to vary independently. These realizations also accounted for uncertainties of the plane's strikes, dips, and rakes by varying these angles randomly by ±5° with the resulting distributions of the shear τ (**Figure 9a**) and normal (clamping) σ (**Figure 9b**) tractions shown. Plane 2's (see **Table 1**) σ distribution is lower and distinct from that of Plane 1 (see **Table 1**), suggesting it is more susceptible to slip.

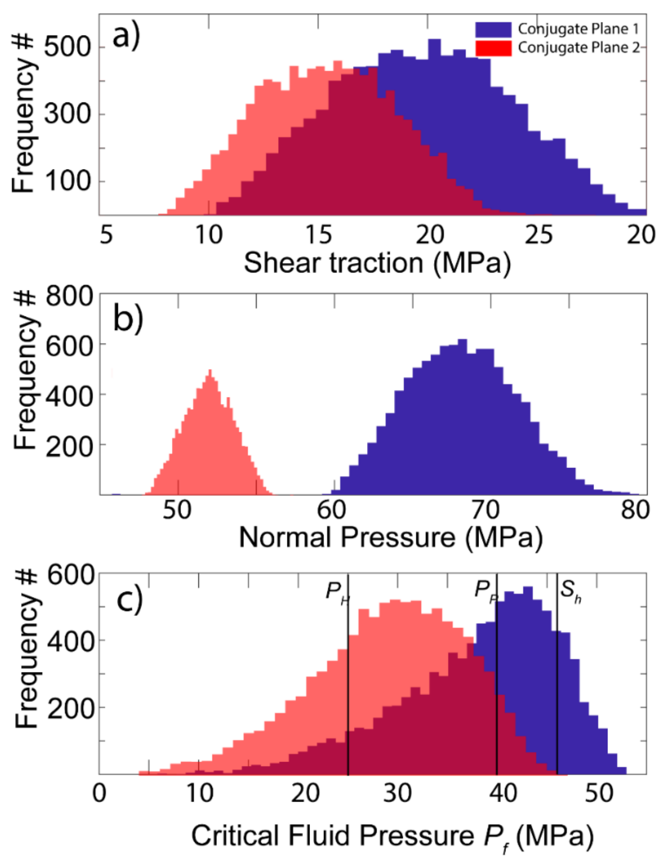

Figure 9. Monte Carlo distributions of **a)** shear traction, **b)** normal clamping traction, and **c)** critical P_f^c required for slip on either *of Event* A*'s* conjugate planes.

3.3 Assess regional susceptibility

It is useful to extend the stress tensor constrained regionally to evaluate slip susceptibility. The magnitude of the deviation of the critical fluid pressure $P_f^c(x,y)$ on the fault plane from the expected ambient $P_P(x,y)$:

$$\Delta P(x,y) = P_P(x,y) - P_f^c(x,y) \tag{12}$$

provides the metric. This measure removes complications from the variable depths (2-4 km) of the Duvernay Formation (and ambient differences in P_P) while indicating the local critical level of pore fluid pressure perturbation necessary to induced slip. Progressively lower values of $\Delta P < 0$ indicate the greater instability. Calculation of the fault's slip-tendency relies on the estimated value of P_f^c that, in turn, requires knowledge of the fault's orientation. *Schwab et al.* [2017], *Stork et al.* [2018], and *Weides et al.* [2014] provide examples of studies that estimate the stability on actual faults or lineaments imaged in 3D reflection seismic volumes, but other studies have used seismicity to outline fault trends [e.g., *Eyre et al.*, 2019; *Jia*, 2019]. To overcome this limitation, we carry out the calculations, with S_h, S_V, P_P, ϕ values calculated in RD_stress.m and S_H using Eqn. 9, over the study area by first assuming that at each mapped point, planes of weakness have the same orientation as the most stable Plane 1 (**Figure 10**) for *Event A* and then, for the sake of comparison, the hypothetical optimally oriented plane along which slip would be most likely. This analysis is also carried out *for Event A*'s Plane 2 but gives similar results; it is unnecessary to show these here. The critical fluid pressure P_f^c is mapped for both Plane 1 (**Figure 10a)** and the optimally oriented plane (**Figure 10b**), followed by the corresponding values of ΔP (**Figures 10c, d, Eqn. 12**) in which the lower the value of ΔP, the greater the susceptibility. Though our earlier slip-tendency analysis suggests faults are unlikely to be oriented in these directions, this analysis does allow for a relative comparison.

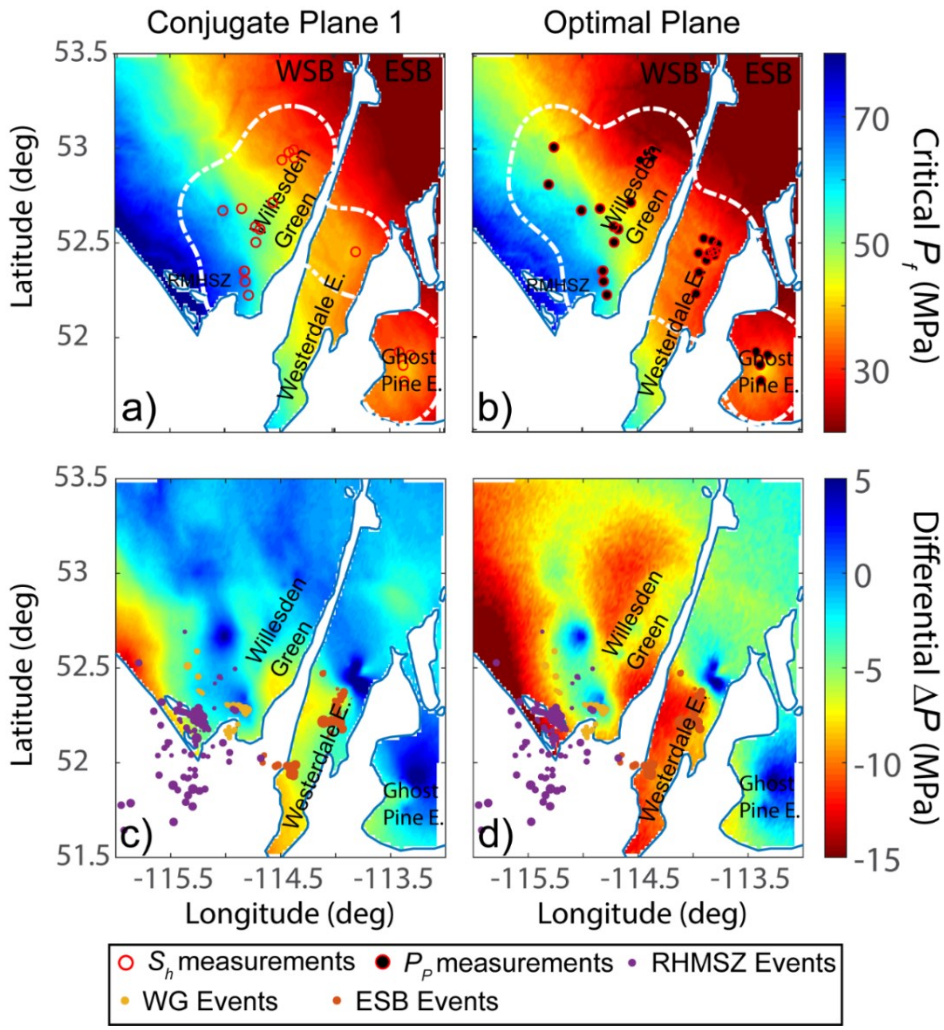

Figure 10. Required critical pressure P_f^c to activate hypothetical faults across the study area for **a)** hypothetical faults across the region oriented parallel to the conjugate Plane 1 for the Red Deer earthquake listed in Table 1, and **b)** assumed faults oriented optimally to slip. **c)** and **d)** are the corresponding pressure difference ΔP (= P_f^c - P_P) shown in a) and b). This analysis is performed on the depths of the Duvernay Formation (2 – 4km from the surface, see **Figure 3b,c**).

We note that many authors instead employ Coulomb failure stress [e.g., *King et al.*, 1994]. We avoid this measure because it necessitates calculation of $\Delta\sigma$ and $\Delta\tau$ requires specific knowledge of the perturbing load and its geometry relative to the vulnerable fault plane [*Catalli et al.*, 2013], information that we do not have at this time. These can often be small, too, relative to the changes in P_f due to injection [e.g., *Segall*, 1985].

4 Discussion

4.1 Comparison of S_h and P_P with Fox Creek area.

An early motivation for this study was to determine whether there are any substantive differences between the stress states in the more seismically active Fox Creek region to the north and the largely aseismic area in the current study. A strike-slip faulting regime is indicated by the observed $S_V > S_h$ and by the observed focal mechanisms in both areas.

Our confidence of the stress orientation ϕ in the areas within the Duvernay Formation area is generally high with stress orientations to the northeast (average $\phi \sim 48°$), which agree with previous studies at much larger scales [*Reiter et al.*, 2014]. The stress orientation to the north in the Fox Creek area shows a similar $\phi \sim 45°$ stress orientation [*Shen et al.*, 2019a].

The secant gradient (stress divided by total depth, see explanation in section 2.3 for details) does not show significant variation between the two areas (**Table 2**). In contrast, however, some differences appear in the tangent gradients of S_h with that for the Fox Creek (32.1 ± 3.1 MPa/km) exceeding that for the current Red Deer study area (22.2 ± 5.6 MPa/km). However, some care must be taken before making a general interpretation as there are some geographic complications between the WSB and ESB. The five S_h values from the East Shale Basin, all at shallower depths from 2157m to 2331m, bias the aggregate slope. Repeating the regression using only the WG values from 2300 m to 3500 m gives an S_h tangent gradient that agrees with that for the Fox Creek area. Though more than 200 km from each other, the Fox Creek and WG zones lie within the WSB and may have similar behavior. Alternatively, this may be due to differences in the depths at which the measurements are made.

Table 2. Comparison of calculated stress and pore pressure gradients between the Fox Creek and Red Deer study areas.

Area	Gradient type	Red Deer			Fox Creek
		Mesozoic[1]	Duvernay Aggregate	Duvernay WG Only	Duvernay[2]
Range of Measurement Depths (km)		1.3-3.0	2.1-3.5	2.3-3.5	2.9-3.9
S_V (MPa/km)	Secant		24.5 ± 0.5		24.5 ± 1.0
S_h (MPa/km)	Secant	16.8 ±3.2	18.3 ± 3.6	18.0 ± 3.3	19.2 ± 2.8
	Tangent	19.1 ± 2.4	22.2 ± 5.6	34.2 ± 6.0	32.1 ± 3.1
P_P (MPa/km)	Tangent		24.8 ± 3.6		29.1±7.2

[1]Reported in *Haug and Bell* [2016]
[2]Reported in *Shen et al.,* [2019a]

Taken together, there does not appear to be significant differences in the S_h and P_P trends between the study areas. However, there are indications that the observed values of S_h within the ESB are elevated relative to the predicted trend. It is important to note that our stress predictions, which rely on kriging of the observed values, retain these local variations. However, it does not appear that the regional differences in S_h and P_p can explain the variations in levels of seismicity between the Fox Creek region and the current study areas.

4.2 Relation to other seismicities in the area

It is useful to contrast this situation with that in the nearby RMHSZ (near 52'12.5'N. 115'15'W), which lies within the deformation belt where, as noted earlier, events were likely associated with sour gas production from Leduc Formation reefs through the 1980s. The foci of these events are reported at depths around 5.2 km [3.2 km below sea level, *Wetmiller*, 1986], with a modest M_W 3.4 (*Event C*, see **Table 1**). The focal mechanism of *Event C* indicates this earthquake occurred on an oblique reverse fault contrasting with the primarily strike-slip focal mechanism for *Event A*.

Using nearby measurements from boreholes compiled by *McLellan* [1989], *Baranova et al.* [1999] provided estimates for the Andersonian stress magnitudes at the depth of *Event C's* focus, obtaining relative $S_V < S_h < S_H$. This is an observation that disagrees with our constraints, which, at this location, predicts a significantly larger S_V such that $S_h < S_V < S_H$. One component of this discrepancy appears to be due to confusion in the use of elevations in *Baranova et al.* [1999] instead of the correct depths reported by *McLellan* [1989], which differ by more than 1 km; as such, their stress model appears to have inadvertently underestimated the S_V magnitudes. Regardless, our observed strike-slip stress state is less consistent with the largely reverse faulting focal mechanism for *Event C*; this may indicate that the stress regime within the disturbed belt differs from that outside of it.

4.3 Implications for the M_W 3.8 earthquake (Event A)

In section 3.2, we showed our calculation of the slip tendency of the fault responsible for *Event A* at different levels of fluid pressures. Examination of **Figures 8a**, **b** suggests that if $P_f \leq P_H$, both conjugate planes are likely to remain clamped (i.e., *SNR* < 0.4). *Eyre et al.* [2019], for example, in their study near Fox Creek, presume that $P_f = P_H$ within the Duvernay Formation and estimate $SNR \sim 0.29$; this would preclude active seismic slip. However, suppose P_f is at the expected ambient formation pore pressure (P_P), provided directly from borehole observations in this study, both conjugate planes are significantly destabilized; the *SNR* for Plane 2, which strikes at 201°, falling outside the $SNR = 0.8$ contour (**Figure 8c**).

One additional point arising from **Figure 8** is that both of *Event A's* possible conjugate planes are not optimally oriented for slip (i.e., 30° from S_H azimuth, assuming $\mu = 0.6$) within the stress field. These results are similar to the conclusions of *Shen et al.* [2019b] for eleven events in the Fox Creek area and a number of the events induced by long-term injection near Prague, Oklahoma, USA [*Cochran et al.*, 2020].

The corresponding critical P_f^c distributions for *Event A's* Plane 1 (**Figure 9c**) is higher than that of Plane 2's, indicating that, again, Plane 2 may slip more easily. The most vulnerable plane is often taken to be that responsible for the earthquake [e.g., *Alt and Zoback*, 2016; *Vavryčuk*, 2014]. This may suggest, but cannot prove, that *Event A* occurred on Plane 2; both distributions have long tails to low P_f. This offers, though improbable, a possibility that slip could be triggered on Plane 2 by pressures as low as 4 MPa. It is helpful to examine **Figure 9c** for some typical values of P_f. Significant fractions of both distributions lie below that expected for the normal hydrostatic gradient $P_f = P_H$, further indicating that slip could initiate even for relatively low fluid pressures.

More interestingly, the Duvernay Formation reservoir at P_P is highly overpressured [*Cochran et al.*, 2020; *Eaton and Schultz*, 2018; *Shen et al.*, 2019b] and more than 90% of Plane 2's P_f^c distribution lies below the ambient P_P. This means that there is a high likelihood of it being unstable, particularly if the fluid pressures are of those expected naturally in the reservoir. In contrast, about 50% of the situations available to Plane 1 also lie below this pressure. Although shown through a more statistical analysis here, this is the same situation as that encountered to the north in the Fox Creek area [*Shen et al.*, 2019b]. There, most of the faults are unstable even at the natural ambient pore pressure. The lack of natural, historical seismicity in the area suggests that the fluid pressures acting along the planes of weakness are likely lower or, though less probable, that the fault cohesion is higher. The Plane 2 distribution in **Figure 9c** does admit stable cases when $P_f = P_P$, but this is not likely. In contrast, about 50% of the cases for Plane 1 remain stable for this condition.

It is also useful to compare the case of $P_f = S_h$. This pressure is a useful reference because S_h is determined from the pressure at which the fracture, artificially created during a transient pressure test and whose plane is presumed to be perpendicular to the S_h direction, is deemed to close [see review in *Schmitt and Haimson*, 2017]. As such, it provides a lower bound to the fluid pressures transmitted into the formation along an artificial fracture and, subsequently, to the fault should a direct hydraulic connection be established. The peaks for both distributions and the entire distribution for Plane 2 fall below S_h, indicating that a fluid pressure approaching S_h would destabilize the fault.

In summary, two points are raised by the analysis of the critical P_f^c distributions in **Figure 9c**. First, the natural reservoir pressure P_P alone is sufficient to destabilize a relatively wide range of appropriately oriented planes of weakness; and the question arises as to why the more natural seismic activity is not present. Second, production-based HF operations at this site must extend the fluid pressures, which exceed S_h to propagate fractures, that can readily provide enough critical P_f to induce slip on both focal mechanism's conjugate planes. This observation is like that from the Fox Creek area [*Shen et al.*, 2019b; *Yaghoubi et al.*, 2020]. A recent contribution from [*Hui et* *al.*, 2021] also provided support that hydraulic communication can potentially be established between wellheads and the fault, raising P_f to the level (greater than P_f^c) needed to move the fault.

More direct comparative examinations of *SNR* (as a function of P_f) reinforce these observations. This is done for both of *Event A's* conjugate planes and the most susceptible, hypothetical optimally oriented plane [see methods in *Shen et al.,* 2019b]. The red and green ribbons represent envelopes for the set of the *SNR* calculations that, respectively, assume cohesions of either $C = 0$ or $C = 5$ MPa. The green ribbon in **Figure 11a**, for example, encompasses possible values of S_H constrained with both borehole failures and focal mechanism inversion with a maximum cohesion of 5 MPa employed. This envelope is superimposed on a gray background that simply highlights the likely range of friction coefficients $0.4 < \mu < 0.8$ to illustrate the P_f for which $SNR > \mu$ such that the fault is most likely to be unstable. As such, the portions of the envelopes above $SNR = 0.8$ and below $SNR = 0.4$ respectively delineate conditions under which the faults are highly likely to be either unstable or stable. We also analyze conjugate Plane 2 (**Figure 11b**) and a hypothetical optimally oriented plane (**Figure 11c**) for comparison. As expected, similar observations are reported, but Plane 2 requires a smaller P_f (even less so for the optimally oriented plane) to reach the unstable $SNR > \mu$.

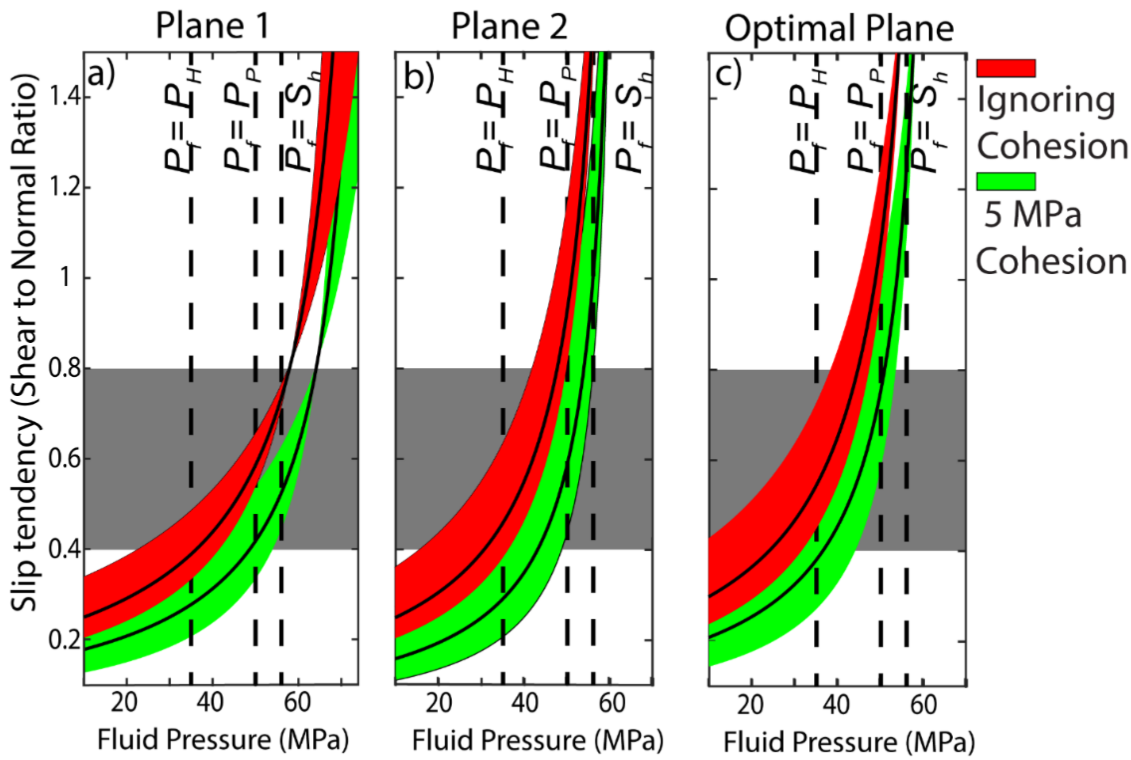

Figure 11. The slip tendency of the **a)** conjugate faulting Plane 1, **b)** Plane 2 of the focal mechanism for the *Event* A, and **c)** a hypothetical fault oriented optimally (assuming $\mu = 0.6$) for slip initiation. Red and green zones represent the range of values calculated for the constrained bounds of S_H (75 – 106 MPa, median 84 MPa), which account for either $C = 0$ or $C = 5$ MPa. The gray box denotes the expected range of μ between 0.4 and 0.8.

In summary, we would like to highlight that the stereographic analysis of **Figure 8** shows that P_f values that make wide ranges of fault orientations susceptible to slip can easily be attained. This suggests that inferring for the stress orientation solely based on the P-T axis described in the earthquake focal mechanism solution may be misleading. Studies using changes in focal mechanism directions during microseismic clusters to claim large changes in stress magnitude and directions need to be carried out with particular care and supported by geomechanical constraints.

This mainly concerns studies that attempt to describe subtle stress variation over a relatively small volume of crust.

4.4 Areal constraints on stability and factors controlling induced seismicity

One major motivation for this analysis is to investigate the correlation between our deterministic susceptibility map using ΔP (see Eqn. 12) as the metric with the locations of the reported seismic clusters, as shown in **Figures 10c, d.**

The Westerdale Embayment has the greatest levels of induced seismicity [*Schultz and Wang*, 2020] and appears to have increasingly negative (less stable) values of ΔP (Eqn. 12). The more northern portions of the Westerdale Embayment as well as the Ghost Pine Embayment, both with lower levels of seismicity, display positive (more stable) ΔP. These correlations suggest that ΔP may be useful in providing a measure of instability.

In contrast, numerous, but small, induced events are detected in the Willesden Green Field [$M_W < 2$, *Schultz and Wang*, 2020], lying immediately to the north of the Rimbey-Meadowbrook Reef Trend. This zone is primarily characterized by positive ΔP (**Figures 10c**, **d**). This low-level seismicity conflicts with the lack of events immediately to the east, where significantly more negative values of ΔP appear in the maps.

There are several possible reasons for this discrepancy. First, to have an induced event, one presupposes the existence of an appropriate plane of weakness upon which sliding may occur. The aseismic zones may simply not have any vulnerable structures upon which sliding is favored. It may also be that such vulnerable structures do exist in these areas, but none of the hydraulic fracturing operations were within range to attain hydraulic connection [*Wilson et al.*, 2018]; the *Event A* (M_W 3.8/M_L 4.2) might happened within such range according to [*Hui et al.,* 2021].

Secondly, the stress and pore pressure measurements may not accurately predict the conditions everywhere within the study area. While we are generally confident in the results that lie within the white boundaries in **Figures 4** and **10**, there are some areas with fewer or no measurements that may rember the extrapolations invalid due to geological complexity. This problem is particularly severe for S_H whose values are constrained with a larger uncertainty. A third possibility is that vulnerable planes of weakness do exist, but stresses may have already been relieved by events prior to the historical record, aseismically, or via many smaller events that are not observed or cataloged.

As such, the relative susceptibility mapping of **Figure 10** should not, without further information, be interpreted directly to indicate zones where induced earthquakes will/would occur, but rather provide additional constraints on the risks associated with a given perturbation in pressure. It would be useful to build on this analysis by comparing it against actual hydraulic fracturing pressure records. More specifically, how do the actual pressures attained during hydraulic fracture stimulations compare to the estimated P_f^c? Might the pressures employed in the aseismic eastern portion of the Willesden Green Field be lower than those used near the cluster of seismicity? Addressing these questions is beyond the scope of the current study; it is unknown whether the appropriate data even exists or could be accessed, but carrying out such an examination would test the validity of this stability analysis.

That human activities might initiate earthquakes has been known since the middle of the last century with a great deal of interest in earthquakes stimulated by deep fluid waste injections of the Denver earthquakes [e.g., *Healy et al.*, 1968], from crustal loading of large surface hydroelectric reservoirs [e.g., *Gough and Gough*, 1970; *Gupta*, 2018], due to stimulation and operation of geothermal reservoirs [e.g., *Zang et al.*, 2014], hydrocarbon energy production [e.g., *Suckale*, 2009; *Wetmiller*, 1986], long term disposal of water or greenhouse gases [e.g., *Ellsworth*, 2013] and hydraulic fracture stimulation [e.g., *Atkinson et al.*, 2016; *Fasola et al.*, 2019; *Schultz et al.*, 2020].

Extensive literature supplying hypotheses has been developed to explain the mechanisms causing such induced earthquakes. However, virtually all of these require that the effective state of stress resolved on the vulnerable fault plane to sufficiently perturbed and overcome the Coulomb frictional resistance, whether it be a static value or a derived from a time-dependent rate-state model. This may be accomplished by locally modifying the state of total stress from the imposition of the new load nearby or by reducing the effective compressive normal traction σ by increasing the fluid pressure P_f [e.g., *Garagash and Germanovich*, 2012]. Recent experimental investigations also suggested that the effective initial stress also controls the rupture velocities and, thus, the earthquake types (i.e., seismic or aseismic; [*Passelègue et al.*, 2020]). Studies attempting to explain the responsible mechanism usually focus on one or the other as being primarily responsible. However, changes in both should be expected to contribute to greater or lesser extents.

Different types of perturbing loads have also been invoked. Some studies employ analytic elastic dislocation solutions [e.g., *Green and Sneddon*, 1950; *Pollard and Segall*, 1987; *Warpinski*, 2000] to calculate the stress field generated by a fluid-filled hydraulic fracture that is superposed to the existing stress field and resolved onto a fracture plane [e.g., *Kettlety et al.*, 2020]. Other models have calculated the perturbing stresses using poroelastic analytic [e.g., *Baranova et al.*, 1999; *Goebel et al.*, 2017; *Segall*, 1985; *Segall and Lu*, 2015], or numerical [e.g., *Cueto-Felgueroso et al.*, 2018; *Deng et al.*, 2016] solutions. Depending on the availability of fluid pathways in the reservoir, pressure changes due to fluid diffusion are important as well [e.g., *Shapiro and Dinske*, 2009]. They may explain the delays in seismicity in some cases [e.g., *Baisch et al.*, 2010].

Our fault stability analyses show that the active fluid pressure P_f is likely the most crucial factor, given that the expected natural pore pressures are already at ~90% of S_h. This indicates that even before anthropogenic perturbation, both conjugate slip surfaces for *Event* A were critically loaded. Consequently, the problem in trying to target the mechanisms ultimately responsible for triggering the slip, in this case, is that only small perturbations in σ, τ, and P_f might be required; this confounds clear discrimination of which factors are most important. One can easily devise various mechanical earth models that would favor one or the other mechanisms. However, hydraulic fracturing introduces fluid pressures that often significantly exceed S_h [e.g., *Kleiner and Aniekwe*, 2019]. The low matrix permeabilities of the rocks within and surrounding the Duvernay Formation and many other unconventional shale oil/gas reservoirs likely preclude diffusive fluid pressure transfers; and fluid pressures need to be transmitted via more permeable natural fractures systems [*Lele et al.*, 2017; *MacKay et al.*, 2018]. In contrast, induced poroelastic changes from a fracture are relatively modest in comparison [*Baranova et al.*, 1999; *Deng et al.*, 2016; *Goebel et al.*, 2017], suggesting that direct hydraulic connectivity may be the most important component in these cases [*Lele et al.*, 2017].

5 Conclusions

On the basis of the lack of seismicity, the current study area was initially assessed as low seismic risk [*Pawley* et al., 2018]. Recent earthquakes are related to hydraulic fracturing operations motivate further analysis. A more deterministic analysis that includes a geomechanical evaluation of fault slip tendency is required to assist in explaining both the prior lack of seismicity and the recent events.

We develope a quantitative 3D stress distribution model that estimates the quantitative absolute Andersonian stress tensor (S_H, S_h, $S_{V,}$ and ϕ). The ambient pore fluid pressure P_P from borehole logs and transient pressure tests within the Duvernay Formation. We apply these data to study the mechanical stability of the two possible conjugate fault planes associated with the Red Deer earthquake of March 2019. Both planes would remain stable if the fluid pressure acting on the fault P_f were at the P_H. However, both are unstable if P_f is at the ambient natural pore fluid pressure P_P as determined from the borehole measurements. This apparent natural instability conflicts with the area's historical lack of seismicity and, correspondingly, evidence for large deformations. One possible reason for the lack of natural seismicity may be that the higher pore pressures observed in the rock's matrix may be dissipated by enhanced permeability along steeply dipping faults should they be present [*Shen et al.*, 2019b].

Motivated by such findings, we subsequently perform susceptibility analysis for the study area using both the critical P_f^c needed to activate a fault and its difference to the expected ambient P_P ($\Delta P = P_f^c$ - P_P) as metrics. These suggest that the Ghost Pine Embayment to the southeast and the northern part of the Westerdale Embayment are generally stable (requires $P_f^c > P_P$ to be activated). This finding agrees with the general absence of earthquakes reported from seismological observations. The Red Deer (March 2019) earthquake happened in a zone we considered to be less stable owing to the high P_P measured and interpolated with transient wellbore fluid tests.

This study used quantitative measures of stress and pore pressure to assess the geomechanical stability of fault planes linked to induced hydraulic fractures. These data are then extended to provide maps of susceptibility using a metric proportional to the deviation between the ambient pore pressure and that required to initiate slip. Mostly, but not entirely, this measure of susceptibility correlated with the observed levels of induced seismicity. The reasons for this are unknown, but it is possible that the presence or absence of real planes of weakness, or the proximity of them to hydraulic fracturing operations, may play a role.

Acknowledgments and Data

L. W. Shen and T. E. Hauck's contributions to this work are supported by the Alberta Energy Regulator. M. Babakhani is thanked for providing the cross-section image in **Figure 1**. Earlier components of D. R. Schmitt's contribution are supported by the NSERC at the University of Alberta and currently through the Stephen and Karen Brand Professor and Purdue University. In compliance with the AGU FAIR policy, data including the transient well testing results, the borehole image log analysis results, and the Matlab program RD_stress.m are accessible through *Shen and Schmitt* [2020] at http://dx.doi.org/10.17632/tgmxx5vkjx.1

References

Alberta Energy Regulator, (2015), Subsurface order no. 2: Monitoring and reporting of seismicity in the vicinity of hydraulic fracturing operations in the Duvernay zone, Fox Creek, Alberta, *[Available at http://www.aer.ca/documents/bulletins/Bulletin-2015-07.pdf]. 3 pages*.

Alberta Energy Regulator, (2019), Subsurface order no. 7, *[Available at https://static.aer.ca/prd/documents/orders/subsurface-orders/SO7.pdf]. 4 pages*.

Alt, R. C., and M. D. Zoback (2016), In situ stress and active faulting in Oklahoma, *Bull. Seismol. Soc. Amer.*, *107*(1), 216-228.

Ameen, M.S., (2016), Fracture modes in the Silurian Qusaiba shale play, northern Saudi Arabia and their geomechanical implications. *Marine and Petroleum Geology*, 78, pp.312-355.

Ameen, M.S., (2019), April. Borehole imaging of natural fractures and stress indicators in the Jurassic Carbonate Shale Plays, Eastern Saudi Arabia. In Sixth EAGE Shale Workshop (Vol. 2019, No. 1, pp. 1-5). *European Association of Geoscientists & Engineers.*

Amontons, G., (1695), Remarques et experiences physiques sur la construction d'une nouvelle clepsydre, sur les barometees, les thermometres et les hygrometres, Paris.

Amontons, G., (1699), Moyen de substituer commodement l'action du feu, a la force des hommes et des cheveaux pour mouvoir les machines. *Histoire de l'Académie royale des sciences*, pp.112-126.

Anderson, E. M. (1951), *The dynamics of faulting and dyke formation with applications to Britain*, Oliver and Boyd.

Atkinson, G. M., D. W. Eaton, H. Ghofrani, D. Walker, B. Cheadle, R. Schultz, R. Shcherbakov, K. Tiampo, J. Gu, and R. M. Harrington (2016), Hydraulic fracturing and seismicity in the Western Canada Sedimentary Basin, *Seismological Research Letters*, *87*(3), 631-647.

Atkinson, G. M., Eaton, D.W. and Igonin, N., 2020. Developments in understanding seismicity triggered by hydraulic fracturing. *Nature Reviews Earth & Environment*, 1(5), pp.264-277.

Baisch, S., R. Vörös, E. Rothert, H. Stang, R. Jung, and R. Schellschmidt (2010), A numerical model for fluid injection induced seismicity at Soultz-sous-Forêts, *International Journal of Rock Mechanics and Mining Sciences*, *47*(3), 405-413.

Baranova, V., A. Mustaqeem, and S. Bell (1999), A model for induced seismicity caused by hydrocarbon production in the Western Canada Sedimentary Basin, *Canadian Journal of Earth Sciences*, *36*(1), 47-64.

Barton, C. A., M. D. Zoback, and K. L. Burns (1988), In-situ stress orientation and magnitude at the Fenton Geothermal Site, New Mexico, determined from wellbore breakouts, *Geophysical Research Letters*, *15*(5), 467-470.

Beaumont, C. (1981), Foreland basins, *Geophysical Journal International*, *65*(2), 291-329.

Bell, J., and S. Bachu (2003), In situ stress magnitude and orientation estimates for Cretaceous coal-bearing strata beneath the plains area of central and southern Alberta, *Bulletin of Canadian Petroleum Geology*, *51*(1), 1-28.

Bell, J., and G. Caillet (1994), A reinterpretation of the stress regime of the Aquitaine basin, southwestern France, and implications for hydrocarbon recovery, in *Hydrocarbon and Petroleum Geology of France*, edited, pp. 209-219, Springer.

Bell, J., and D. Gough (1979), Northeast-southwest compressive stress in Alberta evidence from oil wells, *Earth and planetary science letters*, *45*(2), 475-482.

Bell, J., and S. Grasby (2012), The stress regime of the Western Canadian sedimentary basin, *Geofluids*, *12*(2), 150-165.

Bank of Montreal, (2019), East of the reef - Duvernay Oil Play, in *BMO Capital Markets - Energy - A & D Advisory*, edited.

Bott, M. H. P. (1959), The mechanics of oblique slip faulting, *Geological Magazine*, *96*(2), 109-117.

Bouzidi, Y., D. R. Schmitt, R. A. Burwash, and E. R. Kanasewich (2002), Depth migration of deep seismic reflection profiles: crustal thickness variations in Alberta, *Canadian Journal of Earth Sciences*, *39*(3), 331-350.

Burwash, R., C. McGregor, and J. Wilson (1994), Precambrian Basement Beneath the Western Canada Sedimentary Basin, Geological Atlas of the Western Canada sedimentary Basin, 49-56, *Alberta Research Council*.

Byerlee, J., 1978. Friction of rocks. In Rock friction and earthquake prediction (pp. 615-626). *Birkhäuser, Basel.*

Castaños, H., and C. Lomnitz (2002), PSHA: Is it science?, *Engineering Geology*, *66*(3-4), 315-317.

Catalli, F., M. A. Meier, and S. Wiemer (2013), The role of Coulomb stress changes for injection-induced seismicity: The Basel enhanced geothermal system, *Geophysical Research Letters*, *40*(1), 72-77.

Chen, Y., Y. J. Gu, C. A. Currie, S. T. Johnston, S.-H. Hung, A. J. Schaeffer, and P. Audet (2019), Seismic evidence for a mantle suture and implications for the origin of the Canadian Cordillera, *Nature communications*, *10*(1), 1-10.

Chopra, S., R. K. Sharma, A. K. Ray, H. Nemati, R. Morin, B. Schulte, and D. D'Amico (2017), Seismic reservoir characterization of Duvernay shale with quantitative interpretation and induced seismicity considerations—A case study, *Interpretation*, *5*(2), T185-T197.

Cochran, E. S., R. J. Skoumal, D. McPhillips, Z. E. Ross, and K. M. Keranen (2020), Activation of optimally and unfavourably oriented faults in a uniform local stress field during the 2011 Prague, Oklahoma, sequence, *Geophysical Journal International*, *222*(1), 153-168.

Corlett, H., R. Schultz, P. Branscombe, T. Hauck, K. Haug, K. MacCormack, and T. Shipman (2018), Subsurface faults inferred from reflection seismic, earthquakes, and sedimentological relationships: Implications for induced seismicity in Alberta, Canada, *Marine and Peroleum Geology*, *93*, 135-144.

Coulomb, C. A. (1773), Sur une application des regles de maximis & minimis a quelques problemes de statique, relatifs a I' architecture. *Memoires de Mathematique & de Physique, presentes a I' Academie. Royale des Sciences par divers Savans, & Ius dans ses Assemblees*, 7: 343–382

Cueto-Felgueroso, L., C. Vila, D. Santillán, and J. C. Mosquera (2018), Numerical Modeling of Injection-Induced Earthquakes Using Laboratory-Derived Friction Laws, *Water Resources Research*, *54*(12), 9833-9859.

Deng, K., Y. Liu, and R. M. Harrington (2016), Poroelastic stress triggering of the December 2013 Crooked Lake, Alberta, induced seismicity sequence, *Geophysical Research Letters*, *43*(16), 8482-8491.

Eaton, B.A. (1969), Fracture gradient prediction and its application in oilfield operations. *Journal of petroleum technology*, 21(10), pp.1-353.

Eaton, B.A. (1975), January. The equation for geopressure prediction from well logs. In *Fall meeting of the Society of Petroleum Engineers of AIME*. Society of Petroleum Engineers.

Eaton, D. W., N. Igonin, A. Poulin, R. Weir, H. Zhang, S. Pellegrino, and G. Rodriguez (2018), Induced Seismicity Characterization during Hydraulic-Fracture Monitoring with a Shallow-Wellbore Geophone Array and Broadband Sensors, *Seismological Research Letters*, *89*(5), 1641-1651.

Eaton, D. W., and R. Schultz (2018), Increased likelihood of induced seismicity in highly overpressured shale formations, *Geophysical Journal International*, *214*(1), 751-757.

Eberhart-Phillips, D., and D. H. Oppenheimer (1984), Induced seismicity in The Geysers geothermal area, California, *Journal of Geophysical Research: Solid Earth*, *89*(B2), 1191-1207.

Edwards, D. J., and R. J. Brown (1999), Understanding the influence of Precambrian crystalline basement on Upper Devonian carbonates in central Alberta from a geophysical perspective, *Bulletin of Canadian Petroleum Geology*, *47*(4), 412-438.

Ekpo, E., D. Eaton, and R. Weir (2017), Basement Tectonics and Fault Reactivation in Alberta Based on Seismic and Potential Field Data, in *Geophysics*, edited, IntechOpen.

Ellsworth, W. L. (2013), Injection-induced earthquakes, *Science*, *341*(6142), 1225942.

Ellsworth, W.L., Giardini, D., Townend, J., Ge, S. and Shimamoto, T., 2019. Triggering of the Pohang, Korea, earthquake (M w 5.5) by enhanced geothermal system stimulation. Seismological Research Letters, 90(5), pp.1844-1858.

Eyre, T. S., D. W. Eaton, M. Zecevic, D. D'Amico, and D. Kolos (2019), Microseismicity reveals fault activation before M w 4.1 hydraulic-fracturing induced earthquake, *Geophysical Journal International*, *218*(1), 534-546.

Fasola, S. L., M. R. Brudzinski, R. J. Skoumal, T. Langenkamp, B. S. Currie, and K. J. Smart (2019), Hydraulic fracture injection strategy influences the probability of earthquakes in the Eagle Ford shale play of South Texas, *Geophysical Research Letters*, *46*(22), 12958-12967.

Frankel, A. (2013), Comment on "Why earthquake hazard maps often fail and what to do about it" by S. Stein, R. Geller, and M. Liu, *Tectonophysics*, *592*, 200-206.

Galloway, E., T. Hauck, H. Corlett, D. Pană, and R. Schultz (2018), Faults and associated karst collapse suggest conduits for fluid flow that influence hydraulic fracturing-induced seismicity, *Proceedings of the National Academy of Sciences*, *115*(43), E10003-E10012.

Garagash, D. I., and L. N. Germanovich (2012), Nucleation and arrest of dynamic slip on a pressurized fault, *Journal of Geophysical Research: Solid Earth*, *117*(B10).

Goebel, T., M. Weingarten, X. Chen, J. Haffener, and E. Brodsky (2017), The 2016 Mw5. 1 Fairview, Oklahoma earthquakes: Evidence for long-range poroelastic triggering at> 40 km from fluid disposal wells, *Earth and Planetary Science Letters*, *472*, 50-61.

Gough, D., and W. Gough (1970), Load-induced earthquakes at Lake Kariba—II, *Geophysical Journal International*, *21*(1), 79-101.

Green, A., and I. Sneddon (1950), The distribution of stress in the neighbourhood of a flat elliptical crack in an elastic solid, paper presented at *Mathematical Proceedings of the Cambridge Philosophical Society*, Cambridge University Press.

Gu, Y. J., and L. Shen (2015), Noise correlation tomography of southwest western Canada sedimentary basin, *Geophysical Journal International*, *202*(1), 142-162.

Gupta, H. K. (2018), Reservoir triggered seismicity (RTS) at Koyna, India, over the past 50 yrs, *Bull. Seismol. Soc. Amer.*, *108*(5B), 2907-2918.

Hardebeck, J. L., and E. Hauksson (2001), Crustal stress field in southern California and its implications for fault mechanics, *Journal of Geophysical Research: Solid Earth*, *106*(B10), 21859-21882.

Haug, K. and Bell, J.S. (2016), Compilation of in situ stress data from Alberta and Northeastern British Columbia (tabular data, tab delimited). *Alberta Energy Regulator, AER/AGS Digital Data*, *40*, p.2016.

Healy, J., W. Rubey, D. Griggs, and C. Raleigh (1968), The denver earthquakes, *Science*, *161*(3848), 1301-1310.

Heidbach, O., M. Rajabi, K. Reiter, M. Ziegler, and WSM team (2016), World stress map database release 2016, *GFZ Data Services*, *10*.

Hincks, T., W. Aspinall, R. Cooke, and T. Gernon (2018), Oklahoma's induced seismicity strongly linked to wastewater injection depth, *Science*, *359*(6381), 1251-1255.

Hoffman, P. F. (1988), United plates of America, the birth of a craton: Early Proterozoic assembly and growth of Laurentia, *Annual Review of Earth and Planetary Sciences*, *16*(1), 543-603.

Hui, G., Chen, S., Gu, F., Pang, Y., Yu, X. and Zhang, L. (2021), Insights on controlling factors of hydraulically induced seismicity in the Duvernay East Shale Basin. *Geochemistry, Geophysics, Geosystems*, *22*(2), p.e2020GC009563.

Jaeger, J.C. and N.G.W., Cook (1976), Fundamentals of Rock Mechanics 2nd ed., 585. *Halsted, London*.

Jia, S. Q. (2019), Stress Inversion and Damage Quantification in Tight Gas Shale with Application to Hydraulic Fracturing. M.Sc. thesis, University of Calgary.

Kettlety, T., J. Verdon, M. Werner, and J. Kendall (2020), Stress transfer from opening hydraulic fractures controls the distribution of induced seismicity, *Journal of Geophysical Research: Solid Earth*, *125*(1), e2019JB018794.

King, G. C., R. S. Stein, and J. Lin (1994), Static stress changes and the triggering of earthquakes, *Bull. Seismol. Soc. Amer.*, *84*(3), 935-953.

Kleiner, S., and O. Aniekwe (2019), The Duvernay shale completion journey, paper presented at *SPE Kuwait Oil & Gas Show and Conference*, Society of Petroleum Engineers.

Lele, S., T. Tyrrell, and G. Dasari (2017), Geomechanical analysis of fault reactivation due to hydraulic fracturing, paper presented at *51st US Rock Mechanics/Geomechanics Symposium*, American Rock Mechanics Association.

Lemieux, S. (1999), Seismic reflection expression and tectonic significance of Late Cretaceous extensional faulting of the Western Canada Sedimentary Basin in southern Alberta, *Bulletin of Canadian Petroleum Geology*, *47*(4), 375-390.

Liu, L., and M. D. Zoback (1992), The effect of topography on the state of stress in the crust: application to the site of the Cajon Pass Scientific Drilling Project, *Journal of Geophysical Research: Solid Earth*, *97*(B4), 5095-5108.

MacKay, M. K., D. W. Eaton, P. K. Pedersen, and C. R. Clarkson (2018), Integration of outcrop, subsurface, and microseismic interpretation for rock-mass characterization: An example from the Duvernay Formation, Western Canada, *Interpretation*, *6*(4), T919-T936.

Maury, V., J.-R. Grassob, and G. Wittlinger (1992), Monitoring of subsidence and induced seismicity in the Lacq gas field (France): the consequences on gas production and field operation, *Engineering Geology*, *32*(3), 123-135.

Marone, C. (1998), Laboratory-derived friction laws and their application to seismic faulting. *Annual Review of Earth and Planetary Sciences, 26*(1), pp.643-696.

McClure, M. W., and R. N. Horne (2011), Investigation of injection-induced seismicity using a coupled fluid flow and rate/state friction model, *Geophysics*, *76*(6), WC181-WC198.

McLellan, P. (1989), *In-situ stress magnitudes from hydraulic fracturing treatment records: a feasibility study*, Institute of Sedimentary and Petroleum Geology.

Michael, A. J. (1984), Determination of stress from slip data: faults and folds, *Journal of Geophysical Research: Solid Earth*, *89*(B13), 11517-11526.

Moore, P. F. (1988), Devonian reefs in Canada and some adjacent areas.

Morris, A., D. A. Ferrill, and D. B. Henderson (1996), Slip-tendency analysis and fault reactivation, *Geology*, *24*(3), 275-278.

Mukuhira, Y., C. Dinske, H. Asanuma, T. Ito, and M. Häring (2017), Pore pressure behavior at the shut-in phase and causality of large induced seismicity at Basel, Switzerland, *Journal of Geophysical Research: Solid Earth*, *122*(1), 411-435.

Ong, O. N., D. R. Schmitt, and R. S. Kofman (2015), Seismic anisotropy and uniaxial stress measurements on Duvernay sedimentary rocks in Alberta: Report submitted to AER Core Research Laboratory, 28 pp, Alberta Geological Survey, Edmonton.

Pană, D. I., and B. A. van der Pluijm (2015), Orogenic pulses in the Alberta Rocky Mountains: Radiometric dating of major faults and comparison with the regional tectono-stratigraphic record, *GSA Bulletin*, *127*(3-4), 480-502.

Passelègue, F. X., M. Almakari, P. Dublanchet, F. Barras, J. Fortin, and M. Violay (2020), Initial effective stress controls the nature of earthquakes, *Nature Communications*, *11*(1), 1-8.

Pawley, S., R. Schultz, T. Playter, H. Corlett, T. Shipman, S. Lyster, and T. Hauck (2018), The geological susceptibility of induced earthquakes in the Duvernay play, *Geophysical Research Letters*, *45*(4), 1786-1793.

Peters, S. E., and R. R. Gaines (2012), Formation of the 'Great Unconformity' as a trigger for the Cambrian explosion, *Nature*, *484*(7394), 363-366, doi:10.1038/nature10969.

Pollard, D.D. and P. Segall (1987), Theoretical displacements and stresses near fractures in rock: with applications to faults, joints, veins, dikes, and solution surfaces. In *Fracture mechanics of rock*, pp. 277-347.

Preston, A., G. Garner, K. Beavis, O. Sadiq, and S., Stricker (2016), Duvernay reserves and resources report: A comprehensive analysis of Alberta's foremost liquids-rich shale resource, *Alberta Energy Regulator, Calgary*, 83.

Price, R. (2001), An evaluation of models for the kinematic evolution of thrust and fold belts: structural analysis of a transverse fault zone in the Front Ranges of the Canadian Rockies north of Banff, Alberta, *Journal of Structural Geology*, *23*(6-7), 1079-1088.

Rebollar, C., E. Kanasewich, and E. Nyland (1982), Source parameters from shallow events in the Rocky Mountain House earthquake swarm, *Canadian Journal of Earth Sciences*, *19*(5), 907-918.

Reiter, K., O. Heidbach, D. Schmitt, K. Haug, M. Ziegler, and I. Moeck (2014), A revised crustal stress orientation database for Canada, *Tectonophysics*, *636*, 111-124.

Rokosh, C., J. Pawlowicz, H. Berhane, S. Anderson, and A. Beaton (2009), What is shale gas? An introduction to shale-gas geology in Alberta, *Energy Resource Conservation Board*

(2008-08), available at: http://ags. gov. ab. ca/publications/abstracts/OFR_2008_08. html.

Ross, G., and D. Eaton (1999), Basement reactivation in the Alberta Basin: Observational constraints and mechanical rationale, *Bulletin of Canadian Petroleum Geology*, *47*(4), 391-411.

Ross, G., R. Parrish, M. Villeneuve, and S. Bowring (1991), Geophysics and geochronology of the crystalline basement of the Alberta Basin, western Canada, *Canadian Journal of Earth Sciences*, *28*(4), 512-522.

Schmitt, D. R. (2014), Basic geomechanics for induced seismicity: A tutorial, *CSEG Recorder (Nov 2014)*, *39*(11), 20-27.

Schmitt, D. R., C. A. Currie, and L. Zhang (2012), Crustal stress determination from boreholes and rock cores: Fundamental principles, *Tectonophysics*, *580*, 1-26.

Schmitt, D. R., and B. Haimson (2017), Hydraulic fracturing stress measurements in deep holes, *Rock Mechanics and Engineering Volume 1: Principles*, 183.

Schultz, R., G. Atkinson, D. Eaton, Y. Gu, and H. Kao (2018), Hydraulic fracturing volume is associated with induced earthquake productivity in the Duvernay play, *Science*, *359*(6373), 304-308.

Schultz, R., R. J. Skoumal, M. R. Brudzinski, D. Eaton, B. Baptie, and W. Ellsworth (2020), Hydraulic Fracturing-Induced Seismicity, *Reviews of Geophysics*, *58*(3), e2019RG000695.

Schultz, R., V. Stern, Y. J. Gu, and D. Eaton (2015), Detection threshold and location resolution of the Alberta Geological Survey earthquake catalogue, *Seismological Research Letters*, *86*(2A), 385-397.

Schultz, R., and R. Wang (2020), Newly emerging cases of hydraulic fracturing induced seismicity in the Duvernay East Shale Basin, *Tectonophysics*, 228393.

Schultz, S., J. A. MacEachern, and H. D. Gibson (2019), Late Mesozoic reactivation of Precambrian basement structures and their resulting effects on the sequence stratigraphic architecture of the Viking Formation of east-central Alberta, Canada, *Lithosphere*, *11*(3), 308-321.

Schwab, D. R., T. S. Bidgoli, and M. H. Taylor (2017), Characterizing the Potential for Injection-Induced Fault Reactivation Through Subsurface Structural Mapping and Stress Field Analysis, Wellington Field, Sumner County, Kansas, *Journal of Geophysical Research: Solid Earth*, *122*(12).

Segall, P. (1985), Stress and subsidence resulting from subsurface fluid withdrawal in the epicentral region of the 1983 Coalinga earthquake, *Journal of Geophysical Research: Solid Earth*, *90*(B8), 6801-6816.

Segall, P., and S. Lu (2015), Injection-induced seismicity: Poroelastic and earthquake nucleation effects, *Journal of Geophysical Research: Solid Earth*, *120*(7), 5082-5103.

Seithel, R., E. Gaucher, B. Mueller, U. Steiner, and T. Kohl (2019), Probability of fault reactivation in the Bavarian Molasse Basin, *Geothermics*, *82*, 81-90.

Shapiro, S. A., and C. Dinske (2009), Fluid-induced seismicity: Pressure diffusion and hydraulic fracturing, *Geophys. Prospect.*, *57*(2), 301-310.

Shen, L., D. Schmitt, and K. Haug (2018), Measurements of the States of In Situ Stress for the Duvernay Formation near Fox Creek, West-Central Alberta*Rep.*, 29 pp, Alberta Energy Regulator / Alberta Geological Survey.

Shen, L., D. Schmitt, and K. Haug (2019a), Quantitative constraints to the complete state of stress from the combined borehole and focal mechanism inversions: Fox Creek, Alberta, *Tectonophysics*, *764*, 13, doi:https://doi.org/10.1016/j.tecto.2019.04.023.

Shen, L., D. Schmitt, and R. Schultz (2019b), Frictional Stabilities on Induced Earthquake Fault Planes at Fox Creek, Alberta: A Pore Fluid Pressure Dilemma, *Geophysical Research Letters*, *46*(15), 9, doi:10.1029/2019GL083566.

Shen, L., and D. Schmitt (2020), Data for: States of in-situ stress in the Duvernay East Shale Basin and Willesden Green of Alberta, Canada: variable in-situ stress states effect fault stability, Mendeley Data, V1, doi: 10.17632/tgmxx5vkjx.1

Stein, S., R. Geller, and M. Liu (2011), Bad assumptions or bad luck: Why earthquake hazard maps need objective testing, *Seismological Research Letters*, *82*(5), 623-626.

Stein, S., R. J. Geller, and M. Liu (2012), Why earthquake hazard maps often fail and what to do about it, *Tectonophysics*, *562*, 1-25.

Stork, A., C. Nixon, C. Hawkes, C. Birnie, D. White, D. Schmitt, and B. Roberts (2018), Is CO2 injection at Aquistore aseismic? A combined seismological and geomechanical study of early injection operations, *Int. J. Greenh. Gas Control*, *75*, 107-124.

Streit, J. E., and R. R. Hillis (2004), Estimating fault stability and sustainable fluid pressures for underground storage of CO2 in porous rock, *Energy*, *29*(9-10), 1445-1456.

Suckale, J. (2009), Induced seismicity in hydrocarbon fields, in *Advances in geophysics*, edited, pp. 55-106, Elsevier.

Townend, J., and M.D. Zoback (2000), How faulting keeps the crust strong. *Geology*, *28*(5), pp.399-402.

Valley, B., and K. F. Evans (2019), Stress magnitudes in the Basel enhanced geothermal system, *International Journal of Rock Mechanics and Mining Sciences*, *118*, 1-20, doi:10.1016/j.ijrmms.2019.03.008.

van Thienen-Visser, K., and J. Breunese (2015), Induced seismicity of the Groningen gas field: History and recent developments, *The Leading Edge*, *34*(6), 664-671.

Vavryčuk, V. (2014), Iterative joint inversion for stress and fault orientations from focal mechanisms, *Geophysical Journal International*, *199*(1), 69-77.

Wallace, R. E. (1951), Geometry of shearing stress and relation to faulting, *The Journal of geology*, *59*(2), 118-130.

Walsh, F. R., and M. D. Zoback (2016), Probabilistic assessment of potential fault slip related to injection-induced earthquakes: Application to north-central Oklahoma, USA, *Geology*, *44*(12), 991-994.

Warpinski, N. R. (2000), Analytic crack solutions for tilt fields around hydraulic fractures, *Journal of Geophysical Research: Solid Earth*, *105*(B10), 23463-23478.

Weides, S. N., I. S. Moeck, D. R. Schmitt, and J. A. Majorowicz (2014), An integrative geothermal resource assessment study for the siliciclastic Granite Wash Unit, northwestern Alberta (Canada), *Environ. Earth Sci.*, *72*(10), 4141-4154.

Weir, R. M., D. W. Eaton, L. R. Lines, D. C. Lawton, and E. Ekpo (2018), Inversion and interpretation of seismic-derived rock properties in the Duvernay play, *Interpretation-a Journal of Subsurface Characterization*, *6*(2), SE1-SE14, doi:10.1190/int-2017-0149.1.

Wetmiller, R. J. (1986), Earthquakes near Rocky Mountain House, Alberta, and their relationship to gas production facilities, *Canadian Journal of Earth Sciences*, *23*(2), 172-181.

Wilson, M., F. Worrall, R. Davies, and S. Almond (2018), Fracking: How far from faults?, *Geomechanics and Geophysics for Geo-Energy and Geo-Resources*, *4*(2), 193-199.

Woodland, D., and J. Bell (1989), In situ stress magnitudes from mini-frac records in Western Canada, *Journal of Canadian Petroleum Technology*, *28*(05).

Yaghoubi, A., M. Dusseault, S. Mahbaz, and Y. Leonenko (2020), Probabilistic Injection-Induced Fault Slip Assessment in Fox Creek Alberta, paper presented at *54th US Rock Mechanics/Geomechanics Symposium*, American Rock Mechanics Association.

Zang, A., V. Oye, P. Jousset, N. Deichmann, R. Gritto, A. McGarr, E. Majer, and D. Bruhn (2014), Analysis of induced seismicity in geothermal reservoirs–An overview, *Geothermics*, *52*, 6-21.

Zoback, M.D. (2010), Reservoir geomechanics. Cambridge University Press.